P-ISSN: 2798-1134 | E-ISSN: 2797-3549 | DOI: 10.52562/injoes.2023.795

Indonesian Journal of Earth Sciences

https://journal.moripublishing.com/index.php/injoes

| Research Article |

A New Method for Selecting the Phase and Group Velocity Dispersion Curves of Rayleigh and Love Surface Waves: Real Data Case of Central Anatolia, Turkey (Türkiye)

Özcan Çakır[1]*, Yusuf Arif Kutlu[2]

[1]*Department of Geophysics, Süleyman Demirel University, Isparta, Türkiye*
[2]*Department of Geophysics, Çanakkale Onsekiz Mart University, Çanakkale, Türkiye*
**Correspondence: ozcancakir@sdu.edu.tr*

Received: 25 July 2023 / Accepted: 01 October 2023 / Published: 04 October 2023

Abstract: We propose a new method to select the dispersion curve of Rayleigh and Love surface waves obtained from local and regional earthquakes. This method is efficient for the crustal tomography studies and the Central Anatolia is chosen to test it. The single-station method utilizing both seismograms and accelerograms is used for the group velocities from local earthquakes while the two-station approach utilizing the cross correlograms is employed for the group and phase velocities using both local and regional earthquakes. The proposed method is made of two stages. The first stage based on the multiple filter technique – MFT is designed for an automatic selection of the desired dispersion curve. In case of the single-station approach, the MFT diagrams are computed for both Rayleigh and Love seismograms or accelerograms. An algorithm based on several selection criteria is employed to extract the corresponding group velocity dispersion curve from the MFT diagram. In case of the two-station method, the MFT diagrams are computed for both Rayleigh and Love cross correlograms. The latter algorithm developed for the MFT diagram is again applied to the cross correlogram to select the respective two-station group velocity dispersion curve. To select the corresponding two-station phase velocity dispersion curve, another algorithm is developed where the joint inversion of phase and group velocities is employed. The ERROR value quantifying the misfit between the selected and inverted dispersion curves is found minimum when the selected phase velocity curve is compatible with the group velocity curve extracted via the MFT. The selection procedures defined up until this point constitute the first stage. In the second stage, phase and group velocity gathering around base pathways is performed. This way it is possible to compute the averages and standard deviations for the observed pathways traversing the similar geology. The outliers determined by using the averages and standard deviations are eliminated from the data set and this elimination is performed for phase and group velocities, separately.

Keywords: Central Anatolia, Crust, Inversion, Surface Wave, Tomography

INTRODUCTION

Rayleigh and Love surface waves acquired from earthquake recordings present substantial amount of waveform information that are frequently employed to invert the seismic velocity structure of the Earth. The waveforms are either directly inverted (i.e., full waveform inversion – Tohti et al., 2022) or treated through a series of processing steps to obtain the phase and group velocity dispersion curves utilized in the inversion (Zhang et al., 2023). We presently follow the latter methodology. The real Earth is composed of three-dimensional (3-D) structural heterogeneity where slowly varying low frequency structure is superimposed by high frequency 3-D structural variations. We deal with the inversion of the low frequency data for the subsurface analysis and treat the effect of the high frequency wave energy (i.e., scattering – Çakır, 2006) as noise, which imposes error on the observed dispersion curves. We propose a new method for the suppression of noise while selecting the observed dispersion curves (phase and group velocity) more effectively and correctly.

The surface waves are made of fundamental plus higher modes where the fundamental mode dispersion curve isolated by suppressing the higher mode interference is mostly employed in the subsurface velocity inversions (Chen et al., 2021). The fundamental mode dispersion curve is also disturbed by multiple arrivals due to off-great-circle propagation (Chen et al., 2018) and scattering from 3-D heterogeneities (Çakır, 2009). Therefore, one must consider the required measures to reduce the

effect of noise on the observed data. We lay out the details of the new method and test its effectiveness by combining broadband and accelerogram stations in the Central Anatolia to determine the phase and group velocity dispersion curves.

Indicated as shaded in the upper panel of Fig. 1, the test area (or the studied region) taking place in the Anatolian plate with complex tectonic history (i.e., dipping slabs, magmatism, metamorphism, fold-and-thrust belts, faults, suture zones and ophiolites – Bartol &Govers, 2014) has a seismologically challenging crust and upper mantle system. The Anatolian plate with approximate geographical boundaries between 26°–45° E and 36°–42° N is covered by several digital, three-component seismographic stations offering an excellent opportunity to put the suggested method on thorough examination. We consider seismic surface wave recordings at several permanent and temporary stations that provide a range of observed data from all over the epicentral distances to study the subsurface velocity distribution (Magrini et al., 2022). We currently utilize both local (inside the studied region) and regional (outside the studied region) earthquakes to collect the surface wave data. The seismic activity in the Central Anatolia is mainly controlled by two intracontinental strike-slip fault zones (Early Pliocene – Krystopowicz et al., 2020). As shown in the lower panel of Fig. 1, the right-lateral Tuzgölü Fault Zone – TGFZ takes place in the west (Yıldırım, 2014) while the left-lateral Central Anatolian Fault Zone – CAFZ extends in the east (Higgins et al., 2015). These two fault zones as well as other small fracture systems in the studied region (Dirik & Goncuoglu, 1996) provided us the needed surface wave data of local origin. The surface wave data of regional origin is due to the global seismicity around and away from the Anatolian plate. The surface wave tomography is commonly used at various scales (i.e., shallow, regional and global) to image the near surface, crustal and upper mantle structures where both Rayleigh and Love surface waves are used (Barmin et al., 2001; Salaün et al., 2012; Kästle et al., 2018; Çakır, 2018 and 2019). The proposed method is particularly effective for the surface wave tomography to determine the crustal and upper mantle shear-wave velocity distribution.

We utilize both single-station (i.e., source-station) and two-station (i.e., station-station) geometries to attain the fundamental mode phase and group velocity dispersion curves. The broad set of surface wave data and the software package used to complete the respective analysis are first described. Each data processing step is explained in detail using both synthetic and real data. The phase and group velocity dispersion curves are jointly considered to invert the crustal and uppermost mantle shear-wave velocities. We share some examples of two-dimensional (2-D) tomographic velocity maps, which are converted into one-dimensional (1-D) shear-wave velocity-depth profiles at selected locations. The current study primarily focuses on the proposed method for the effective selection of dispersion curves. We also briefly share our findings regarding the future work related to the joint analysis of surface waves with the receiver functions and gravity studies.

GEOLOGICAL SETTING

The Anatolian peninsula is surrounded by the Black Sea to the north, the Aegean Sea to the west, the Mediterranean Sea to the south and the combination of Georgian, Armenian and Iranian high lands to the east. Along the Aegean and Cyprus arcs offshore in the easternmost Mediterranean Sea, the African plate is subducting underneath the Anatolian plate (see Fig. 1). Historically this region was once covered by the Neo-Tethys Ocean with northern and southern branches between Laurasia to the north and Gondwana to the south. The Neo-Tethys Ocean was closed during the Cenozoic era and then the widespread Alps-Zagros-Himalaya orogenic belt with mostly east-west extension was created (Dewey & Şengör, 1979; Şengör & Yılmaz, 1981, Faccenna et al., 2014; Schildgen et al., 2014). The Neo-Tethys oceanic domain covered a very large area including Australia in the east, Tibetan and Iran Plateaus in the middle and the Mediterranean Sea in the west. Following the closure of the Neo-Tethys Ocean, the Anatolian plate in the Eastern Mediterranean region was formed by drifting and amalgamation of micro-blocks (northern Pontides, southern Anatolide-Tauride block, and central Kırşehir massif in Fig. 1 – Boztuğ et al., 2008) rifted from the margins of Gondwana and Laurasia (Zhu et al., 2022).

Tectonic structures ranging from active subduction zones (i.e., Aegean and Cyprus arcs) to continent–continent collision (i.e., Bitlis-Zagros Suture Zone – BSZS) and uplift in central and eastern Anatolian platforms characterize the neo-tectonic era (upper panel in Fig. 1). The northern Neo-Tethyan Ocean closed during the late Cretaceous, which was followed by the slab breakoff happened 54 Ma along a suture zone with approximate E-W extension north of ~39.5° latitude. The suture zone generation was accompanied by asthenospheric mantle upwelling through the slab window, granitoid emplacements, ophiolite obductions and plate uplift and exhumation events (Dilek et al., 2009; Boztuğ et al., 2009; Dilek & Altunkaynak, 2007). Starting from the early Miocene the southern branch of the Neo-Tethys Ocean evolved in more complex fashion, i.e., collision between Eurasia and Arabia along

the Bitlis-Zagros Suture (BSZ) zone and northward subduction of the African plate along the Aegean and Cyprian trenches (Dewey et al., 1989; Bozkurt, 2001).

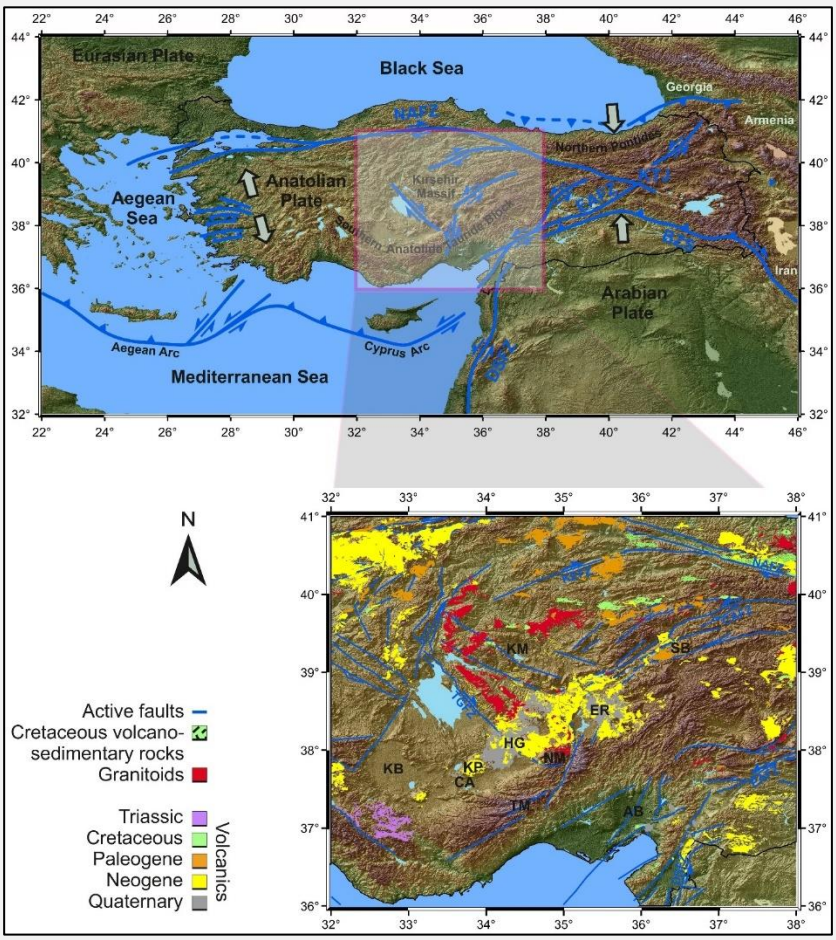

Figure 1. Simplified geological map is presented. The upper map displays the major tectonic features on the Anatolian plate and the surrounding. The relative plate motions are shown by large arrows. The lower map displays the studied region magnified from the upper regional map. The fault zones are shown by blue lines (Duman et al., 2018; Styron & Pagani, 2020). AB stands for Adana Basin; BZS for Bitlis-Zagros Suture; CA for Cinder Cone Area; CAFZ for Central Anatolian Fault Zone; DSFZ for Dead Sea Fault Zone; EAFZ for East Anatolia Fault Zone; KEFZ for Kırıkkale-Erbaa Fault Zone; KB for Konya Basin; KTJ for Karlıova Triple Junction; NAFZ for North Anatolia Fault Zone; KM for Kırşehir Massif; NM for Niğde Massif; SB for Sivas Basin; TGFZ for Tuzgölü Fault Zone; TM for Taurus Mountains. ER (Erciyes), HG (group of Hasandağ, Keçiboyduran and Melendiz) and KP (Karapınar) are major stratovolcanoes (Higgins et al., 2015).

The two major transform faults of the world, i.e., the ~1500 km long E-W trending North Anatolian Fault – NAF and the SSW-NNE trending Eastern Anatolian Fault – EAF, which connects to the Dead Sea Fault to the south, merge at the Karlıova Triple Junction – KTJ at which location the Anatolian plate collides with the Eurasian and Arabian plates (Karaoğlu et al., 2017). These three tectonic features (i.e., NAFZ, EAFZ and KTJ – upper panel in Fig. 1) significantly contribute to the neo-tectonics of Anatolia, which is mainly governed by the Aegean arc to the west and the Bitlis-Zagros Suture (BZS) zone to the east (Uslular & Gençalioğlu-Kuşcu, 2019). The NAFZ and EAFZ as well as other Anatolian fault zones (Barka & Kadinsky-Cade, 1988) under strike-slip conditions create extensional environment along which there exist transtensional pull-apart basins. The network of faults internally deforms the basin deposits and the basement in the Central Anatolian region (lower panel in Fig. 1) where the corresponding seismicity produces earthquakes with focal depths mostly shallower than 40 km (Demirsıkan et al., 2019). The TGFZ with ~135-km length has SW- and NE-dipping fault planes and strikes in the NW-SE direction (Özsayın et al., 2013; Aydar et al., 2021). The CAFZ with ~730 km length and 2–80 km width strikes in the NE-SW direction and continues southward where it intersects the TGFZ (Koçyiğit & Beyhan, 1998).

All these fault zones (i.e., NAFZ, EAFZ, DSFZ, CAFZ and TGFZ) are active producing seismic surface waves utilized in the current study.

In the studied region, there exist several stratovolcanoes (e.g., Hasandağ, Erciyes, Karapınar, Keçiboyduran, and Melendiz – see Aydin, 2008; Güçtekin & Köprübaşi, 2009) with mostly calc-alkaline origin with recent sodic-alkaline component (e.g., Korkmaz et al., 2022). In addition, several small-scale volcanoes (i.e., hundreds of cinder-scoria cones, maars, and domes with mostly basaltic composition) characterize the Quaternary volcanic vents in Central Anatolia (Keller, 1974; Toprak, 1998; Arcasoy, 2001; Uslular et al., 2015; Uslular et al., 2021; Korkmaz et al., 2022).

DATA & METHOD

The Anatolian plate is densely covered by seismograph stations. We consider part of this region (i.e., Central Anatolia) to test the newly proposed method. Both local and distant earthquakes provide efficient azimuthal coverage of wave-paths arriving from almost all directions. Modern seismic waveform data and data processing techniques (Dal Moro & Ferigo, 2011; Herrmann, 2017; Çakır, 2021; Movaghari et al., 2021; Zhou et al., 2022) are utilized where the skin depth of the current surface wave data extends to crustal and uppermost mantle depths.

Surface Wave Data

The studied area with geographic boundaries given by 36.4°–40.6° N and 32.4°–37.6° E is part of the Anatolian plate where hundreds of three-component broadband stations operated by Kandilli Observatory and Earthquake Research Institute (KOERI, 2023) are deployed. For the waveform data, we examined 37 of these stations taking place within boundaries of the present study, but only 27 KOERI stations yielded quality waveform data. The Turkish Disaster and Emergency Management Presidency (AFAD, 2023) has also deployed many seismographic stations to monitor the earthquake activity in the region. We acquired waveforms data from 46 broadband and 98 accelerogram stations from the AFAD repository. Within the scope of the project "Continental Dynamics: Central Anatolian Tectonics – CDCAT" (Abgarmi et al., 2017), 72 three-component broadband stations were installed with recording history from May 2013 to May 2015. Herein we scanned 59 CDCAT stations having locations relevant to this work and acquired quality waveform data for 56 CDCAT stations. The pole-zero files corresponding to broadband stations are used to remove the effect of seismometer impulse response.

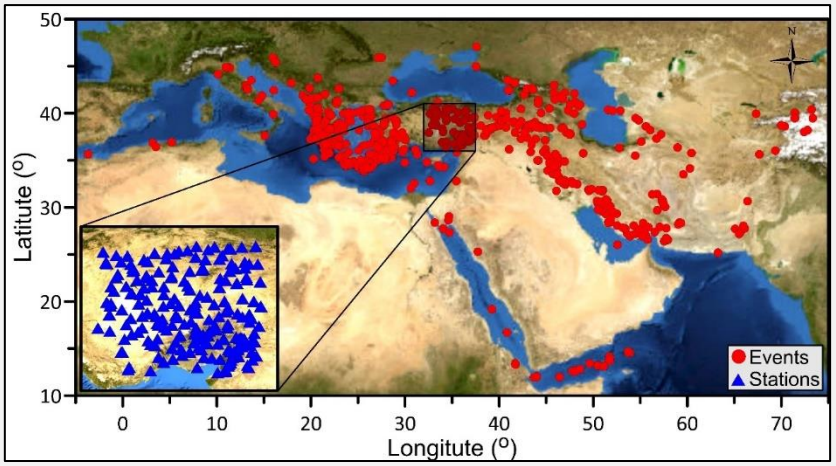

Figure 2. Location map of seismograph stations and events (local and regional earthquakes).

The earthquakes utilized in the dispersion analysis are separated into two groups. These local earthquakes used for the single-station (source-station) analysis take place within the study area (i.e., 36.4°–40.6° N and 32.4°–37.6° E) while these regional earthquakes employed for the two-station (station-station) analysis are selected from the distance range outside the study area. For the single-station events the distance range is set to 100–750 km while for the two-station events the distance range is set to 400–4500 km measured from the center point of the study area. In the meantime, the inter-station distance range used in the station-station analysis is also set to 100–750 km. Earthquakes occurring from year 2005 to year 2023 are scanned in each group and these earthquakes producing good dispersion curves are kept in the data set. For the single- and two-station events the minimum magnitudes are set

to M_w=3.7 and M_w=4.7, respectively while for each group the focal depth range is set to 0–50 km. The source information (i.e., epicenter location, date, origin time, magnitude and depth) for a single-station event is acquired from the AFAD catalog. The United States Geological Survey (USGS, 2023) catalog is utilized to attain the source parameters for the two-station events. After the data selection measures were implemented, we had 227 seismic stations and 914 earthquakes utilized in the source-station and station-station evaluations. Fig. 2 shows the locations of earthquakes and seismic stations on a map. The waveforms belonging to the KOERI and CDCAT stations were downloaded from the web pages of SAGE (SAGE, 2023) while the AFAD homepage is used for the AFAD stations (AFAD, 2023).

The earthquake waveforms are originally delivered in the Vertical/East-West/North-South coordinate system, which is converted to Vertical/Radial/Transverse coordinate system using the theoretical back-azimuth. The Rayleigh and Love surface wave dispersion curves are obtained from the vertical and transverse components, respectively. The observed waveforms are band-pass filtered using the two-way (i.e., phase-free) Butterworth filter with corner frequencies at 0.02 Hz and 0.2 Hz. The propagation effects due to the near-surface complex geology are avoided by filtering the surface waves with frequencies higher than 0.2 Hz. The resultant waveforms are employed to attain both single-station group velocities and two-station phase and group velocities. We should mention that we did not apply any signal-to-noise thresholds to the raw seismic data, but rather restrictions on the magnitude, epicentral distance and focal depth were imposed before extracting dispersion curves. A broad time window is used to cut the raw waveforms from $t_1 = r/8.0$ to $t_2 = r/1.6$ where t_1 and t_2 are the group arrival times (s) computed from the epicentral distance (r) divided by the assumed (maximum – 8.0 km/s and minimum – 1.6 km/s) group velocities. The quality control procedures are strictly applied on the extracted dispersion curves, which are explained in the following sections.

Multiple Filter Technique

We compute the fundamental mode group velocity dispersion curves corresponding to ray-paths between these sources and receivers, i.e., single-station approach. In case of the two-station method, the group velocity curve corresponds to the ray-path between two receivers. The single-station method is applied to a recorded seismogram while the two-station method is applied to a cross-correlogram computed from a couple of seismograms recorded at two aligned seismograph stations. The source and two stations are aligned on a great circle path where the deviation from the alignment is measured by two angles, i.e., $\theta_1 \leq 1^o$ and $\theta_2 \leq 5^o$. Herein θ_1 stands for the azimuthal difference of the source to the two stations and θ_2 defines the azimuthal change between the source to the first station and the first station to the second station (Chen et al., 2018).

The observed surface wave dispersion curve is computed by applying the Multiple Filter Technique – MFT (Herrmann, 2017). The filter function is given by the narrow-band Gaussian filter $\exp[-\alpha\,(f - f_c)^2/f_c^2]$ where f_c denotes the center frequency of the filter. In the filter function, the parameter α controls the filter bandwidth, which determines the resolution when transforming from time domain to frequency domain. Broader frequency band is obtained with smaller α while the corresponding signal in the time domain becomes shorter in duration. We set $\alpha = 16$ after some testing. Our tests show that the observational features of the group velocity curves become smoothed out with smaller α (e.g., $\alpha < 6.25$). On the other hand, disjointed and noisy dispersion curves are obtained with larger α (e.g., $\alpha > 25$), which we do not prefer.

Synthetic Tests for MFT

We consider noise-free synthetic seismograms to check the performance of the MFT on the waveforms to compute the dispersion curves. The theoretical crust and uppermost mantle (Table 1) have the model parameters represented by layer thickness (h), compressional-wave velocity ($V_P^{(0)}$), shear-wave velocity ($V_S^{(0)}$), density (ρ), P-wave quality factor (Q_P), and S-wave quality factor (Q_S). The model structure is 35-km thick above the half-space and includes a low velocity zone in the middle crust. An earthquake with fault plane parameters 45°/45°/45° (Rake/Dip/Strike) is assumed to be observed at these seismograph stations with 270° back-azimuth. The synthetic seismograms utilized in the MFT testing are computed using the software package by Herrmann (2017) where the software is instructed to include at least ten higher modes in the computation. Fig. 3 shows two examples of single-station MFT obtained for the Love surface waves (Figs. 3a and 3b) and Rayleigh surface waves (Fig. 3c and 3d) where the epicentral distance is set to 400 km. In the upper row, the respective modal spectral amplitudes are shown. The fundamental mode energy apparent well above the amplitude level of 0.1 count-sec dominates the amplitude spectrum. In the lower row, the group velocity dispersion image (i.e., MFT

diagram) is represented by a color-coded contour plot on which the overlying white color symbols show the model group velocity dispersion. The fit between the model group velocities and the corresponding MFT picks (i.e., maximums on the group velocity–period profile surfaces) is satisfactory until ~33-s period. The longer period (> 33 s) surface wave amplitudes become smaller at greater epicentral distances (> 400 km), which causes the MFT group velocities lose some precision. The latter precision loss, which is more evident for the Rayleigh surface waves (Fig. 3d), is also related to the source phase shift due to the rupture mechanism of the earthquake (Çakır et al., 2000; Çakır & Erduran, 2001). The higher mode interference is apparently secondary. Therefore, we currently require the inverted single-station surface wave group velocities to have periods shorter than 33-s.

Table 1. The layer parameters for the multi-layered crust and uppermost mantle model structure are listed. The compressional-wave quality factor is set to $Q_P = 2Q_S$. Poisson's ratio is 0.25 and density is computed from $\rho = 0.32V_P^{(0)} + 0.77$ (Berteussen, 1977).

Layer number	h (km)	$V_P^{(0)}$ (km/s)	$V_S^{(0)}$ (km/s)	ρ (gr/cm^3)	Q_S
1	5	4.58	2.65	2.24	200
2	5	5.36	3.10	2.49	200
3	5	6.31	3.65	2.79	200
4	5	6.23	3.60	2.76	200
5	5	5.88	3.40	2.65	200
6	5	6.06	3.50	2.71	200
7	5	6.66	3.85	2.90	200
8	5	7.70	4.45	3.23	400
9	5	7.79	4.50	3.26	400
10	∞	7.87	4.55	3.29	400

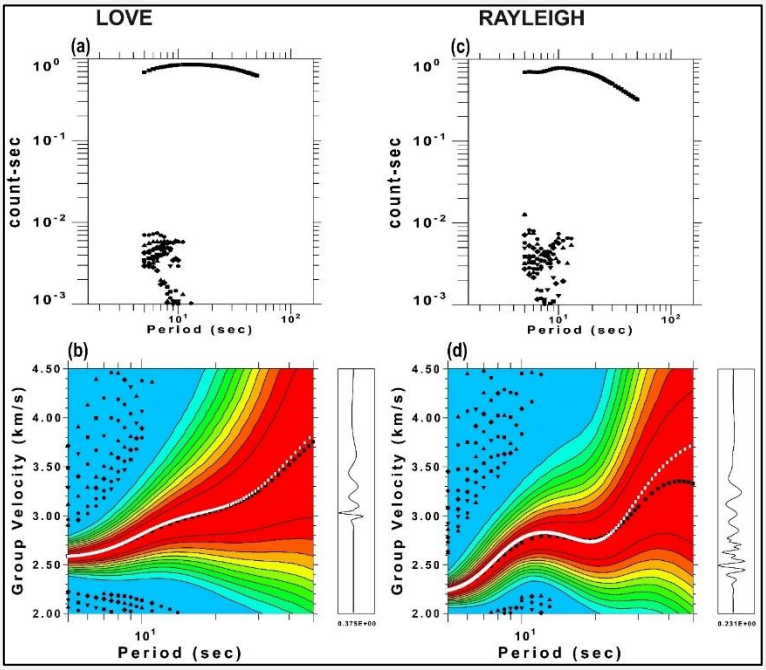

Figure 3. The modal spectral amplitudes for Love (a) and Rayleigh (c) surface waves are shown in the upper row. The single-station group velocity dispersion curves for Love (b) and Rayleigh (d) surface waves are obtained by the application of Multiple Filter Technique – MFT. The black color symbols centering the red color area show the MFT (fundamental mode) group velocities estimated from the waveforms. The group velocities represented by the white color symbols correspond to the theoretical model (Table 1).

In Fig. 4, we show the two-station MFT testing results where the corresponding two stations are assumed to be located at epicentral distances of 2000-km and 2400-km, respectively. The resultant cross-correlogram is computed from two synthetic seismograms at these two stations and is treated by the

MFT algorithm. Since the two stations take place on the same great circle path with the source, the source phase shift is suppressed in the two-station method. The following expression is used to compute the phase velocity $c(\omega)$ from the subsequent cross-correlogram in frequency domain (ω – angular frequency).

$$c(\omega) = \frac{\omega \Delta r}{arctan\{Imag\,[\psi(\omega)]/Real\,[\psi(\omega)]\} + 2n\pi} \quad (1)$$

where the cross-correlogram is defined by the complex function $\psi(\omega)$ and Δr gives the inter-station distance (400 km). In eq 1, the term $2n\pi$ in the denominator may cause ambiguity (i.e., cycle-skipping) in the determination of phase velocity. Below we explain the strategy to avoid the cycle-skipping.

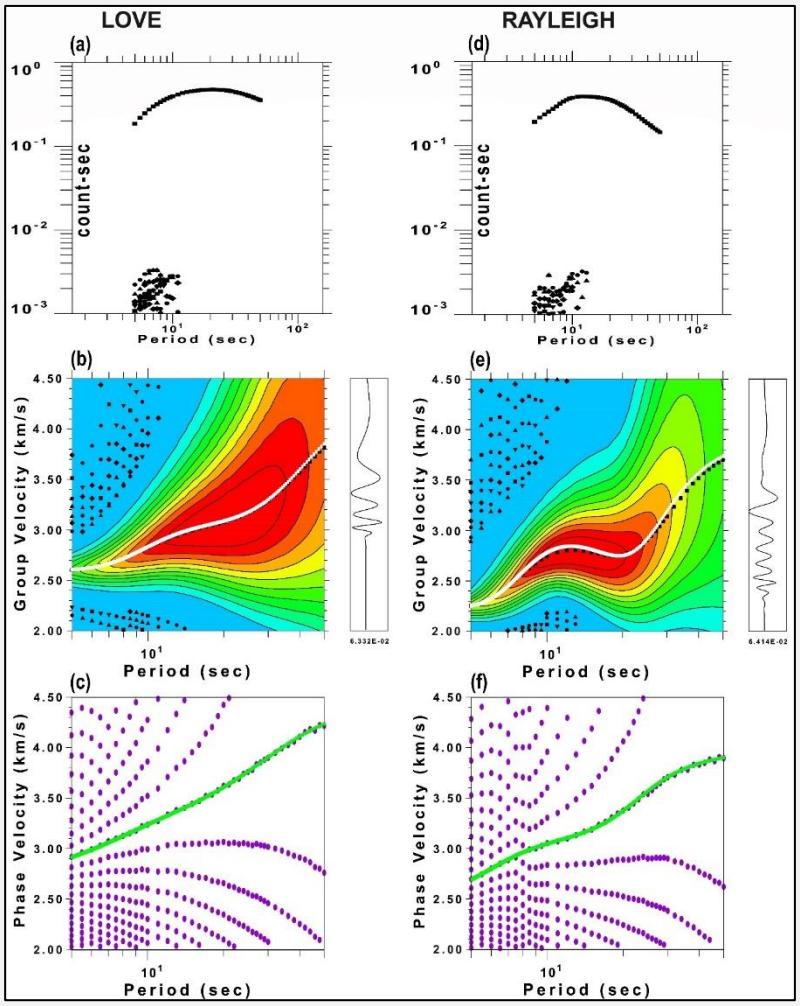

Figure 4. The Modal spectral amplitudes for Love (a) and Rayleigh (d) surface waves are shown in the upper row. The two-station group velocity dispersion curves for Love (b) and Rayleigh (e) surface waves are obtained by the application of Multiple Filter Technique – MFT. The Love (c) and Rayleigh (f) phase velocity plots in the lower row are obtained by the application of Eq. 1. The group and phase velocities corresponding to the theoretical model (Table 1) are depicted by the white and green color symbols, respectively.

Fig. 4 shows two examples of the MFT applied to the Love wave cross-correlogram (Figs. 4a-4c) and Rayleigh wave cross-correlogram (Figs. 4d-4f). In a similar fashion to Fig. 3, we show the respective modal spectral amplitudes in the upper row where the fundamental mode energy is again clear above the amplitude level of 0.1 count-sec. In each panel in the middle row (Figs. 4b and 4e), the two-station MFT group velocity images are shown with the color-coded contour plots. The model (Table 1) group velocities are shown by the white color lines superimposed on the MFT images. The group velocities extracted by the MFT in the period range 5–50 s closely fit the theoretical group velocities even at longer periods, i.e., free of source phase shift (compare to Fig. 3d). The phase velocity calculations by eq 1 are

shown in each panel in the lower row (Figs. 4c and 4f). Each phase velocity panel is made of multiple branch curves resulting from the $2n\pi$ term for different values of n. Therein the theoretical phase velocities are shown by green color lines overlaid on the phase velocity plots. At this point, the correct phase velocity curve must be chosen by setting the correct n value. We first pick a two-station phase velocity curve corresponding to a trial n value. Then we invert this phase velocity curve jointly with the MFT group velocity curve for a one-dimensional shear-wave velocity-depth profile, which should correspond to the average inter-station velocity structure. If the selected two-station phase velocity curve is correct, then the latter inversion ends with minimum error computed from the differences between the observed and inverted dispersion curves. Each station-station pathway in the data set is similarly examined to determine the observed two-station group and phase velocity curves simultaneously. In the following sections, we show examples of phase velocity curve picking applied to the real data.

The synthetic seismograms utilized in the single- and two-station methods described above are shown next to the group velocity MFT diagrams (Figs. 3 and 4). Herein, before applying the MFT algorithm, we boost the weak surface wave spectral amplitudes $|F(\omega)|$ by treating them with the following expression.

$$\bar{F}(\omega) = \frac{|F(\omega)|e^{i\theta(\omega)}}{|F(\omega)|^{\gamma} + \delta} \tag{2}$$

where $\delta = mean|F(\omega)| * 5/100$ is the pre-whitening factor and $\gamma = 0.75$ chosen from the range $0 \leq \gamma \leq 1$. If $|F(\omega)|^{\gamma} \gg \delta$, then $\bar{F}(\omega)$ converges to $F(\omega)$ scaled by δ^{-1} (Wang & Pavlis, 2016). In addition, the software package by Herrmann (2017) utilized to compute the current observational phase velocities include an extra phase term $(\pi/4)$ that needs to be removed. For this reason, the phase velocity computations are corrected using the expression $\tilde{c}(\omega) = \omega\Delta r/(k\Delta r - \pi/4)$ where k is the wave number.

Dispersion Curve Selection

We have developed an automatic two-stage algorithm to select both single-station group velocity curves and two-station phase and group velocity curves for each source-station and station-station pathways, respectively.

First Stage Based on Selection of Individual Dispersion Curves

The single-station and two-station group velocities are selected utilizing the large amplitude surface waves above a threshold set to 20% of the maximum amplitude on the modal spectral amplitude diagram (indicated by orange color dashed lines). Herein the threshold value (20%) is determined based on a trial-and-error approach. For a smaller threshold value (e.g., 10% or 15%), the selection of group velocities on the MFT diagram becomes increasingly more unstable because of smaller surface wave amplitudes, which is not desirable. For a particular station-station pathway, if the group velocity selection procedure fails to find a two-station dispersion curve, then the corresponding phase velocity selection procedure is abandoned. We avoid discontinuities and jumps on the observed dispersion curves. Smooth and one-piece group velocity dispersion curve at least 8-s long is accepted after the selection procedure is applied. If the MFT diagram is made of multiple pieces, then the longest piece is preferred to be recorded into the data set.

Fig. 5 shows the result of the first selection procedure applied to the single station Love surface waves (Figs. 5a and 5b) while these on the right display the same result for the Rayleigh surface waves (Figs. 5c and 5d). The larger modal spectral amplitudes correspond to the fundamental mode energy, i.e., these amplitudes greater than the level marked by the orange color dashed lines (Figs. 5a and 5c). The Multiple Filter Technique – MFT analysis on the seismogram is used to extract the single-station group velocities (white lines in Figs. 5b and 5d) where the respective earthquake parameters are listed in the upper row. The seismograph station is CEYT at 228.7 km epicentral distance. The automatic dispersion selection procedure accepts this MFT result. In Appendix A, we provide the details of the automatic procedure utilized in the selection of the group velocity dispersion curve.

We also apply the MFT to attain the two-station group and phase velocity curves for which the two examples are displayed in Fig. 6. The panels to the left (Figs. 6a-6c) presents the results for the Love surface waves while the panels to the right (Figs. 6d-6f) shows the results for the Rayleigh surface waves. The modal spectral amplitudes greater than the level indicated by the orange color dashed lines (Figs. 6a and 6d) yield the best results for the two-station MFT analysis. The two-station group velocities (white lines) after the MFT analysis on the cross-correlogram are given in the middle row (Figs. 6b and 6e) while the corresponding two-station phase velocities (orange lines) are displayed in the lower row (Figs. 6c

and 6f). The source parameters relevant to the distant earthquake are listed in the upper row. The seismograph station pair is LOD_AT02 with interstation distance of 372.8 km. The period range for the observed two-station dispersion curves is determined from the period range of the observed group velocities. If the latter is less than 8-s, then the corresponding two-station pathway is discarded. The automatic selection procedure for the phase and group velocities accepts this two-station result. Appendix B graphically shows how the automatic selection procedure works on the two-station phase and group velocity dispersion curves. The phase velocity branches corresponding to different n values in $2n\pi$ (see eq 1) are indicated by numbers (i.e., 1, 2, 3 and 4) in Figs. 6c and 6f. These phase velocity branches are utilized in the selection of the correct phase velocity dispersion curve shown in Appendix B.

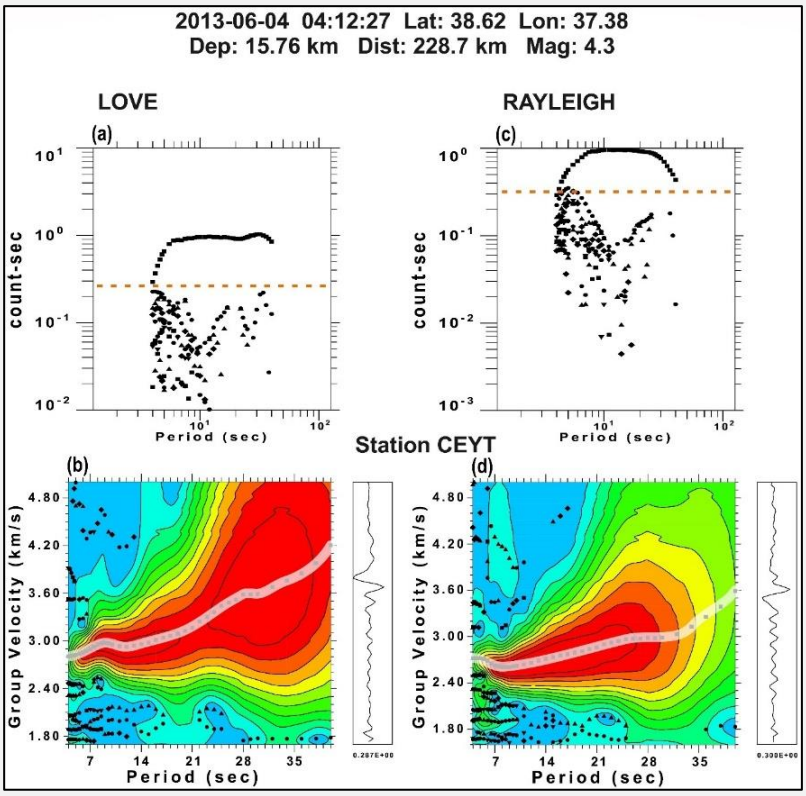

Figure 5. The modal spectral amplitudes for Love (a) and Rayleigh (c) surface waves are shown in the upper row. The dashed orange color line is 20% amplitude threshold. The observed single-station Love (b) and Rayleigh (d) group velocity curves (white lines) are shown for station CEYT.

Second Stage Based on Selection of Group of Dispersion Curves

We apply the second selection procedure to the observed group and phase velocities. The second stage is based on selecting several dispersion curves concurrently satisfying certain pathway conditions. The first stage algorithm above has provided us thousands of observed phase and group velocity dispersion curves. We gather these dispersion curves around some selected (base) pathways so that period-dependent dispersion curve averages and standard deviations can be computed. A gather, which is created for phase and group velocity curves separately, is made of at least three dispersion curves and for each gather an average dispersion curve is computed along with standard deviations. Eventually dispersion curves staying within the error bound given by $\mu \pm 0.08$ km/s (μ – average dispersion) are stored in the accepted data set. In Fig. 7, we show how the base and concurrent pathways are gathered using a two-circle system where the circles have the same radius set to 0.25°. The base pathway (black color) starts from the center of the first circle and ends at the center of the second circle. The remaining pathways (red color) concurrent with the base pathway have the starting location in one circle and the ending location in another circle.

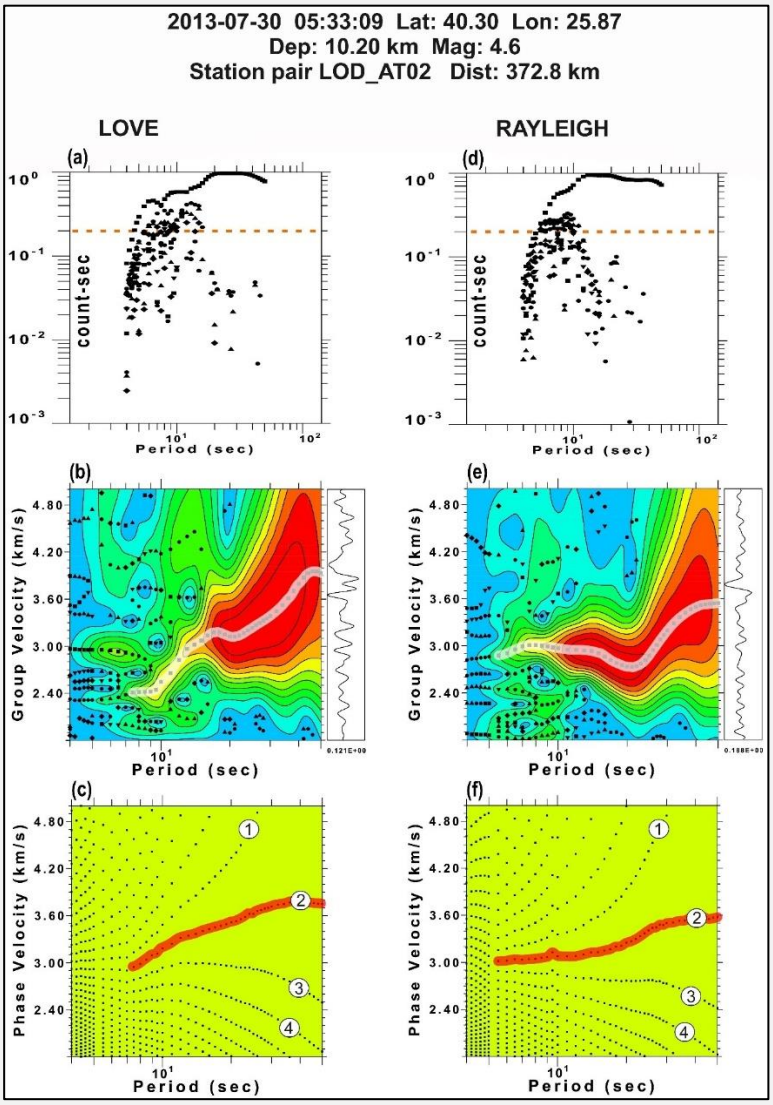

Figure 6. The Modal spectral amplitudes for Love (a) and Rayleigh (d) surface waves are shown in the upper row. The dashed orange color line is 20% amplitude threshold. The observed two-station Love (b) and Rayleigh (e) group velocity (white line – middle row) and Love (c) and Rayleigh (f) phase velocity (orange line – lower row) dispersion curves are shown for a station pair LOD_AT02.

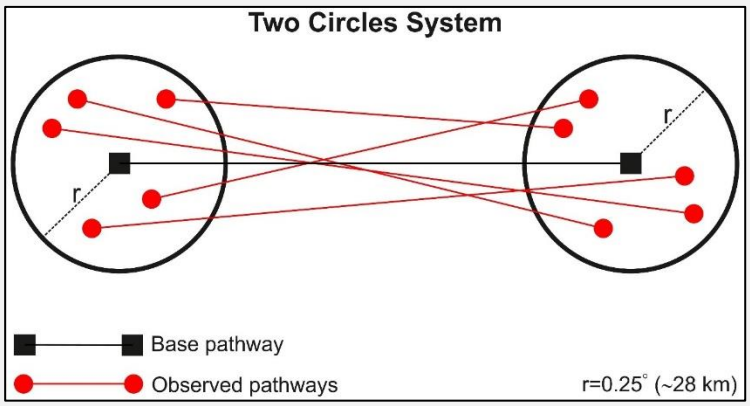

Figure 7. The two-circle system used to gather the nearby observed pathways around the base pathway.

Fig. 8 displays an instance of the second selection procedure applied to a sample base pathway (Rayleigh group velocities), which is given by the black color line connecting two black color symbols in Fig. 8a. The red color lines connecting the red color symbols define the nearby pathways corresponding to the source-station and/or station-station distances. Around the black color symbols, we define two circles each with a radius of 0.25° and then the nearby pathways are required to have both starting and ending points staying within these circles (see Fig. 7). This way we gather several dispersion curves with pathways having geometrical similarity. These curves are supposed to be like each other with minimum deviation because they travel through similar pathways. Fig. 8b shows the corresponding (original) group velocity dispersion curves (purple color) along with the computed averages (μ) and standard deviations (τ) depicted in the green color. If the computed standard deviation is greater than 0.35 km/s, then it is set to 0.35 km/s so that outlying dispersion values are not used in the next step. The dispersion curves staying within the error bound given by $\mu \pm \tau$ are moved to the next step for which the remaining dispersion curves are shown in Fig. 8c. The averages and standard deviations are computed one more time. To avoid the outliers, this time the computed standard deviation is required to be less than 0.25 km/s. For the corresponding pathways given in Fig. 8a, the accepted dispersion curves staying within the newly computed error bound ($\mu \pm \tau$) are shown in Fig. 8d. In the latter step, the computed standard deviations are required to be less than or equal to 0.08 km/s.

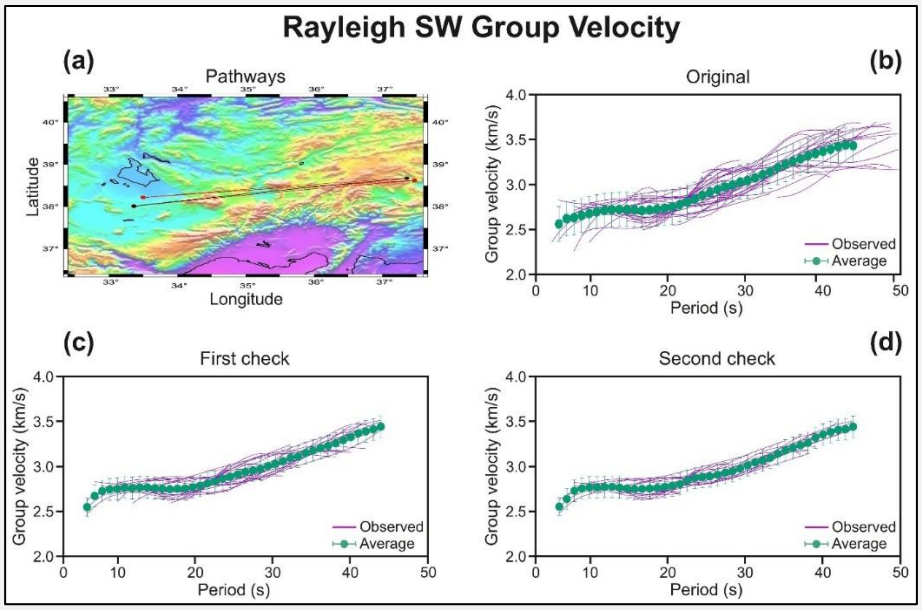

Figure 8. The second selection procedure applied to multiple Rayleigh surface wave group velocity curves are shown. The propagation pathways (a), original dispersion curves (b), the dispersion curves after the first check (c), and the dispersion curves after the second check (d).

The surface wave pathways in Fig. 8a traverse similar geology, but the corresponding dispersion curves (Fig. 8b) show considerable inconsistencies (or ambiguities), which are effectively removed after the second check (Fig. 8d). The ambiguities may result from several effects such as scattering, multiple arrivals, higher mode interference and errors in the determination of source parameters. In Fig. 8, the dispersion curves marked as first check (Fig. 8c) are not accepted as final since some ambiguities remain on the individual dispersion curves and hence the second check (Fig. 8d) is performed. The constraints used in the second selection procedure are set after some trial-and-error runs. Fig. 9 displays another instance of the second selection procedure applied to a sample base pathway created for the Love group velocities. The same second selection procedure is applied to the Rayleigh and Love phase velocities. In Appendix C, Fig. C.1 shows an example of the second selection procedure applied to the Rayleigh phase velocities. Fig. C.2 depicts another example of the second selection procedure prepared for the Love phase velocities. The base pathways currently utilized are constructed from the observed pathways by merging them into several distinct gathers. These dispersion curves not belonging to a gather are automatically removed from the data set.

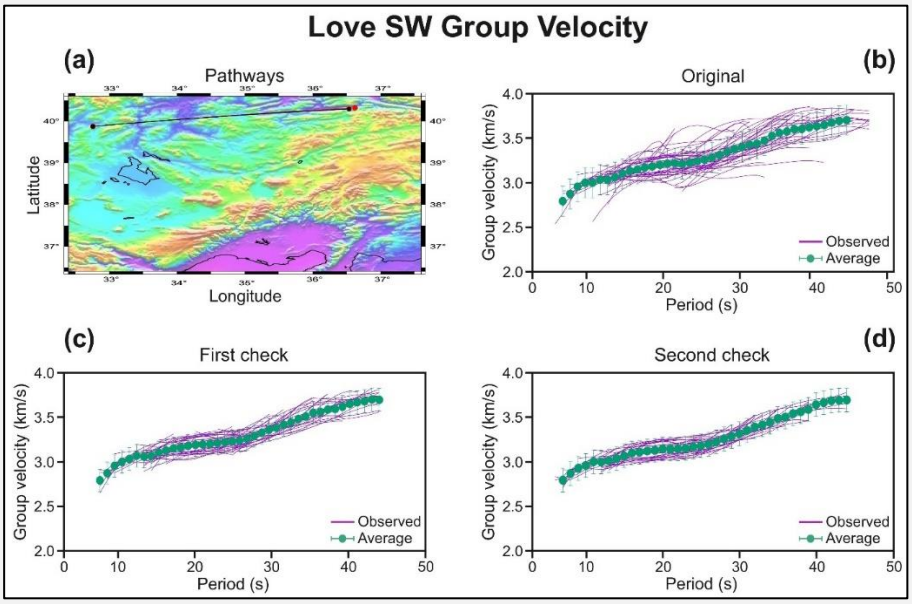

Figure 9. The second selection procedure applied to multiple Love surface wave group velocity curves.

The base pathways are constructed from the original (observed) pathways. A gradual grouping algorithm is applied to the observed pathways where these groups with at least three curves survive to the next step and these groups with two or less curves are dismantled. The next step starts with the surviving pathways and then all the observed group velocity curves are re-grouped with respect to this new set of base pathways. These observed pathways dismantled in the previous step go into their correct group in the re-grouping process. This way the construction of the base pathways is completed, and each dispersion curve is indexed with respect to the base group it belongs to. Fig. 10 shows all these base pathways constructed for the Love and Rayleigh group and phase velocities.

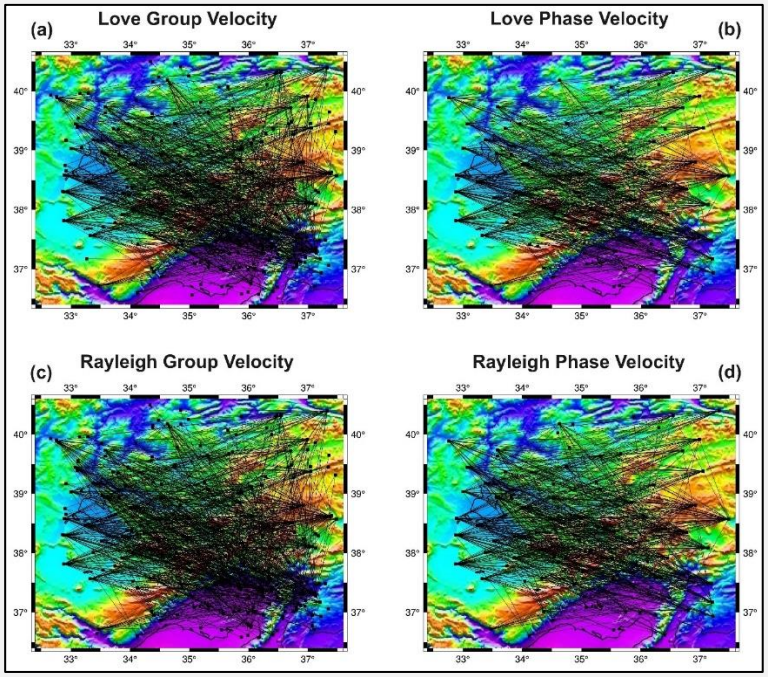

Figure 10. The base pathways used in the second selection procedure are shown for the Love group velocities (a), for the Love phase velocities (b), for the Rayleigh group velocities (c), and for the Rayleigh phase velocities (d).

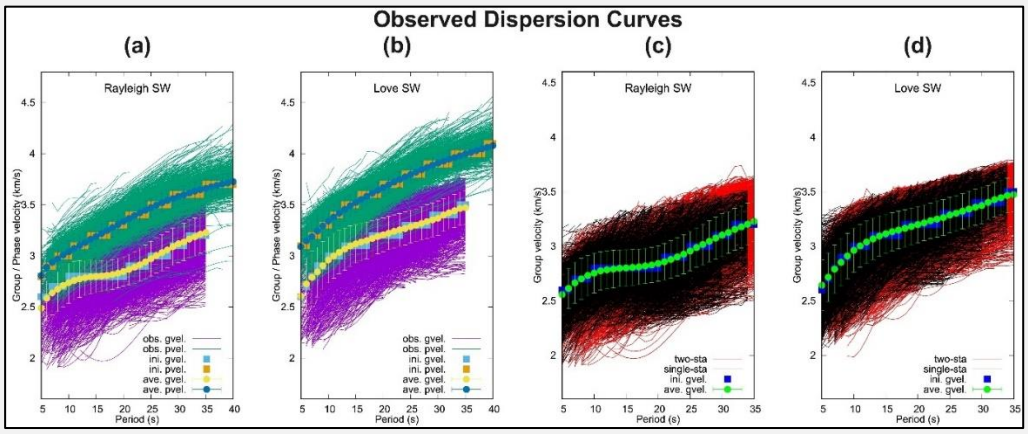

Figure 11. Observed dispersion curves before the selection procedure. First two panels to the left (a and b) give dispersion curves (green color – phase velocity and purple color – group velocity) corresponding to the two-station data. Last two panels (c and d) to the right presents single-station (black color) and two-station (red color) group velocities superimposed on each other. Phase and group velocity averages are indicated by different color solid circles. Different color solid squares indicate group and phase velocities used as initial velocity values in the tomographic inversions.

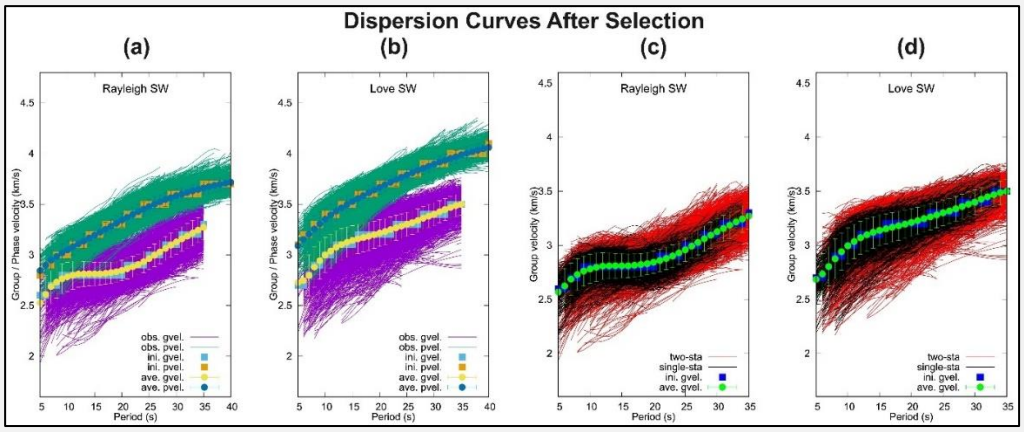

Figure 12. The dispersion curves after the selection procedure.

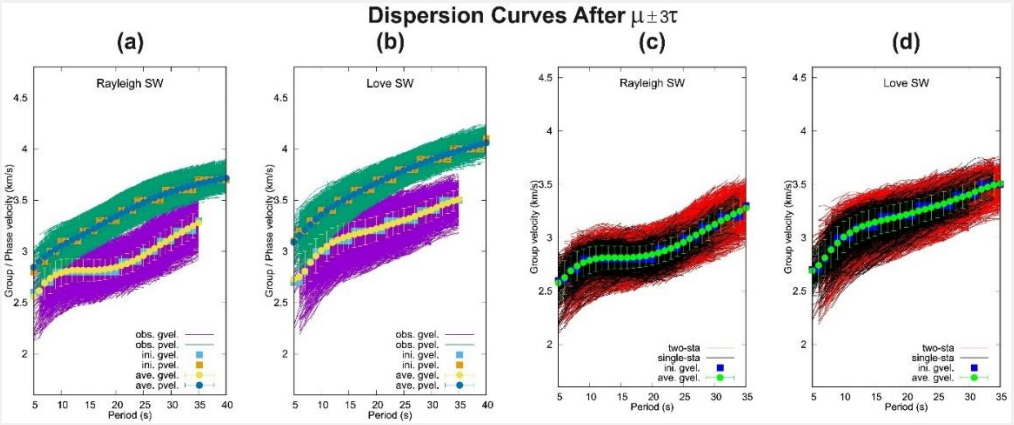

Figure 13. The dispersion curves within the bounds defined by $(\mu \pm 3\tau)$. The averages (μ) and standard deviations (τ) are assumed from these vales given in Fig. 12.

All the observed dispersion curves (Rayleigh and Love group and phase velocities) are presented in Fig. 11. All the accepted dispersion curves after the first and second selection procedures are presented in Fig. 12. Compared to the phase velocities, the group velocities show larger variations around the averages. The computed standard deviations become larger for particularly shorter periods. The latter could be the result of complex near surface geology causing the seismic scattering. The dispersion curves in Fig. 12 show that despite the tight selection criteria imposed during the data quality check there are still some scatterings around the average. We eventually enforce the condition $\mu \pm 3\tau$ (i.e., ~98% confidence interval) on the dispersion curves to get the final dispersion curves depicted in Fig. 13, which are utilized in the tomographic inversions in the following section.

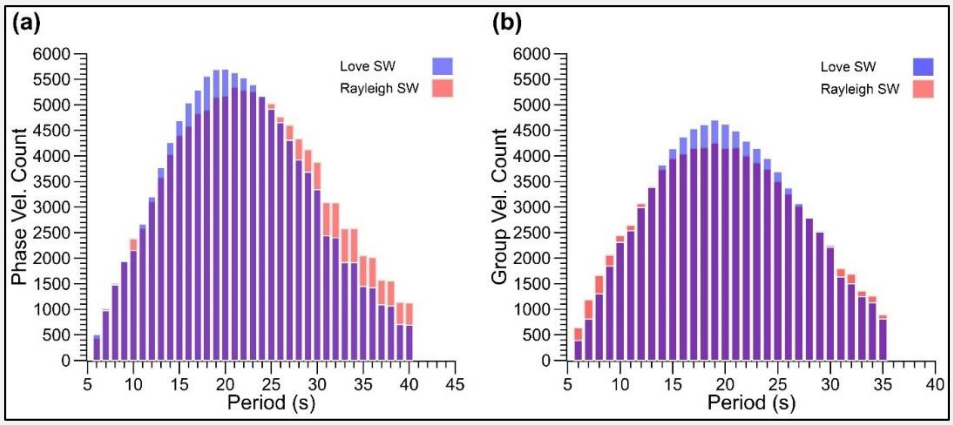

Figure 14. Period dependent phase and group velocity counts based on Rayleigh and Love surface wave dispersion observations shown in Fig. 13. Phase and group velocity counts are shown superimposed.

In Fig. 14, we show the number of observed phase and group velocities at each period (s) where Fig. 14a depicts the phase velocity-period distribution, and Fig. 14b does the same for the group velocities. Around 20-s period, the number of Love surface wave dispersion is more than that for the Rayleigh surface waves although, in the entire period range 6-40 s, the number of Rayleigh surface wave data gets larger (see Table 2). Both Rayleigh and Love surface waves have the highest contribution to the tomography around 20-s period and this contribution gradually diminishes for these surface wave periods shorter or longer than 20 s. In the tomographic inversions discussed below, we consider two different surface wave period ranges. The group velocity data consistent in the period range 7–33 s is considered for the structural inversion while the stable period range for the phase velocities is 7-40 s. Presently the surface waves outside these period ranges have low resolution because of poorer azimuthal coverage due to the lower number of the (selected) observed dispersion curves (Fig. 14). The 33-s group velocity restriction is imposed on the single-station data (see Fig. 3), but the two-station data is free of this restriction (see Fig. 4). According to the sensitivity kernels, the Rayleigh and Love surface waves in the current period range 7-40 s can resolve the shear-wave velocities down to 50-km depth (Agius & Lebedev, 2014; Li et al., 2016). Herein the multi-layered model structure is set to have 48-km thickness above the half-space.

Table 2. Original (observed), accepted and rejected dispersion curves after the second selection procedure.

	Rayleigh Surface Waves		Love Surface Waves	
	Group Velocity	Phase Velocity	Group Velocity	Phase Velocity
Original Dispersion Curves	10898	8770	9836	7819
Accepted Dispersion Curves	5670	7595	5443	6815
Rejected Dispersion Curves	5228	1175	4393	1004

Tomographic Velocity Maps

The surface tomography algorithm employing the fast-marching method (FMM – Sethian & Popovici, 1999; Rawlinson & Sambridge, 2003) is utilized for the current surface wave (group and phase) arrival times tomography where a two-dimensional (2-D) spherical shell coordinate system (latitudes, longitudes) is used. The relevant software package (Rawlinson, 2005) utilized in several tomography studies (e.g., Rawlinson & Sambridge, 2005; Saygin & Kennett, 2010; Fang et al., 2016; Sarjan et al.,

2021) provides several routines for both checkerboard tests (i.e., forward travel times) and 2-D velocity maps (i.e., inverse travel times). The non-linear relationship between velocity and travel time regularized by smoothing and damping is solved iteratively where the background model defined by a grid of nodes with bi-cubic B-spline interpolation is selected from the averages of the observed group and phase velocities (see Fig. 13). The observed surface waves may contend with ray-path-bending due to the heterogeneities in the wave propagating medium, which is considered in the FMM since the travel times are computed for all grid points of the propagating medium, which is essentially different than the raytracing. The differences between the observed and predicted travel times are iteratively reduced using the following objective function $\phi(m)$ (Tarantola, 1987).

$$\phi(m) = [g(m) - d]^T C_d^{-1}[g(m) - d] + \varepsilon[m - m_o]^T C_m^{-1}[m - m_o] + \gamma m^T D^T D m \qquad (3)$$

where the observed and predicted travel times are represented by d and $g(m)$, respectively. The model and data covariance matrices are described by C_m^{-1} and C_d^{-1}, respectively. The damping ($\varepsilon = 0.75$) and smoothing ($\gamma = 1.50$) factors are used to prevent the inverted model (m) from diverging too far from the initial (or background) model (m_o). The inverted model smoothness is implemented by the matrix D. The group and phase velocity maps are obtained by solving eq 3 twice. The latter process is repeated for each surface wave period. The 2-D tomographic velocity maps are constructed on a mesh with size given by 0.05° x 0.05° in latitude and longitude.

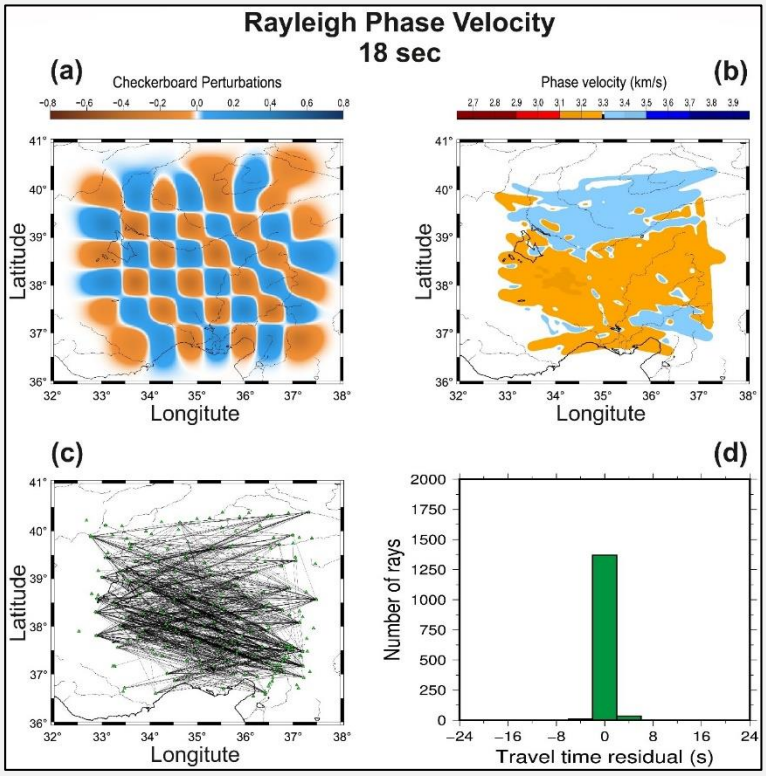

Figure 15. Phase velocity tomography result for 18-s Rayleigh surface waves. The illustration includes 2-D checkerboards (a), 2-D velocity maps (b), 2-D ray-path coverage (c), and travel time residuals (d).

In Fig. 15, we show one example of surface wave tomography result obtained by the application of the tomography source code, which converts the individual dispersion curves into the 2-D velocity maps. Fig. 15 presents the tomography result for the Rayleigh phase velocities with 18-s period. In the figure, checkerboards (Fig. 15a), velocity maps (Fig. 15b), ray-path coverage (Fig. 15c), and travel time residuals (Fig. 15d) are shown. The checkerboard tests along with the ray-path coverage effectively reveal the resolution power of the respective surface wave data. The Rayleigh tomography result shows that the studied region is generally well resolved, but the resolution degrades near the boundaries as indicated by the distorted checkerboard patterns. In Fig. 15, the histogram for the travel time residuals shows that most of the observed ray-paths (> 97%) are fit by the theoretical model within ±2 s. In proportion to

the color scale, the 2-D phase velocity map (Fig. 15b) displays smooth changes from ~3.1 km/s to ~3.5 km/s in the studied region. Generally, the high velocities show up in the north while the low velocities are evident in the south.

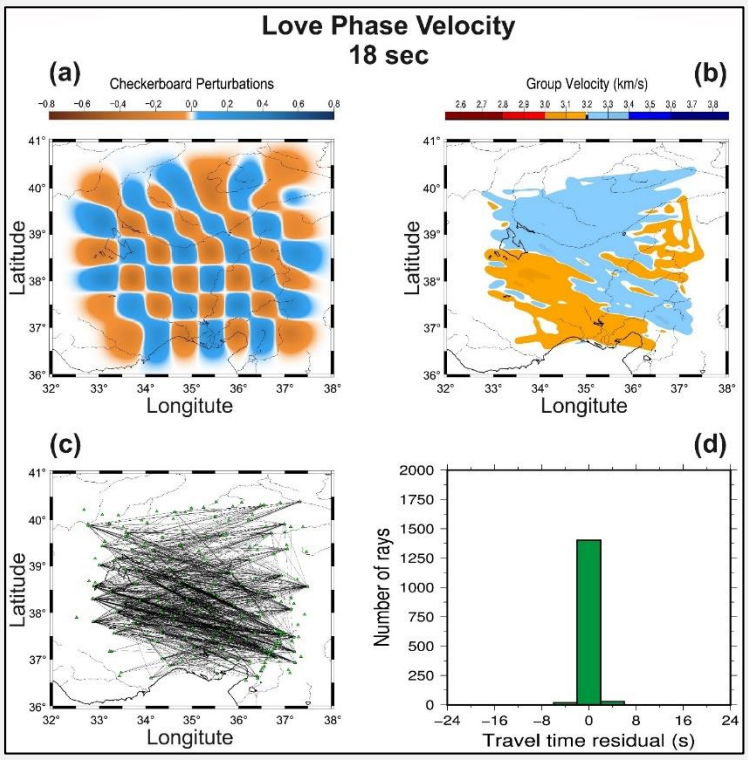

Figure 16. Phase velocity tomography result for 18-s Love surface waves is shown. The illustration includes 2-D checkerboards (a), 2-D velocity maps (b), 2-D ray-path coverage (c), and travel time residuals (d).

In Fig. 16, we show the surface wave tomography result similarly obtained for the Love phase velocities with 18-s period. The presentation style of the tomography result is like these in Fig. 15. The checkerboard tests (Fig. 16a) along with the ray-path coverage (Fig. 16c) show that the Love surface wave phase velocities effectively resolve the studied region, but the resolution power is gradually lost near the boundaries as revealed by the altered checkerboard structures. The histogram for the travel time residuals (Fig. 16d) indicates that majority of the observed ray-paths (> 97%) are theoretically modelled, but with some travel time errors bounded by ± 2 s. In accordance with the phase velocities in Fig. 15, the 2-D phase velocity map (Fig. 16b) shows that the high velocities are generally dominant in the north and that the low velocities show up in the south. In the region around the point (38.5°N – 35.5°E), the Love phase velocities compare to the Rayleigh waves are relatively faster. More surface tomography results for the Rayleigh and Love group velocities at 18-s period are presented in Appendix D (see Figs. D.1 and D.2).

Inverted Velocity-Depth Profiles

To this point, period dependent 2-D group and phase velocity maps are obtained through the surface tomography. We move with the conversion of these 2-D maps into period-dependent group and phase velocity dispersion curves at discrete points defined by a 0.05° x 0.05° – sized grid. Fig. 17 displays one of these points, i.e., 39.2°N, 34.3°E at which location we present the one-dimensional (1-D) shear-wave velocity-depth profiles obtained by the joint inversion of phase (C) and group (U) velocity curves for which the details are provided in Appendix B. Fig. 17a corresponds to the Love surface wave inversion while Fig. 17b gives the inversion result for the Rayleigh surface waves. In Fig. 17, both inversions in the upper row reveal that Rayleigh-and-Love surface wave phase and group velocities are fit well by the corresponding theoretical models (red color velocity-depth profiles). However, these two theoretical models are different from each other, implying anisotropic structure in the subsurface. Fig. 17c shows the inversion result corresponding to the Rayleigh and Love surface wave data jointly inverted. The 1-D velocity-depth profile (green color in Fig. 17d) fails to model all four dispersion curves simultaneously,

i.e., Love-Rayleigh wave discrepancy is implied. Fig. E.1 (Appendix E) presents the 1-D shear-wave velocity-depth profiles at another location in the studied region, i.e., 37.2°N, 35.3°E. The two locations (i.e., 39.2°N, 34.3°E and 37.2°N, 35.3°E) are indicated in Fig. 18a using the red color squares.

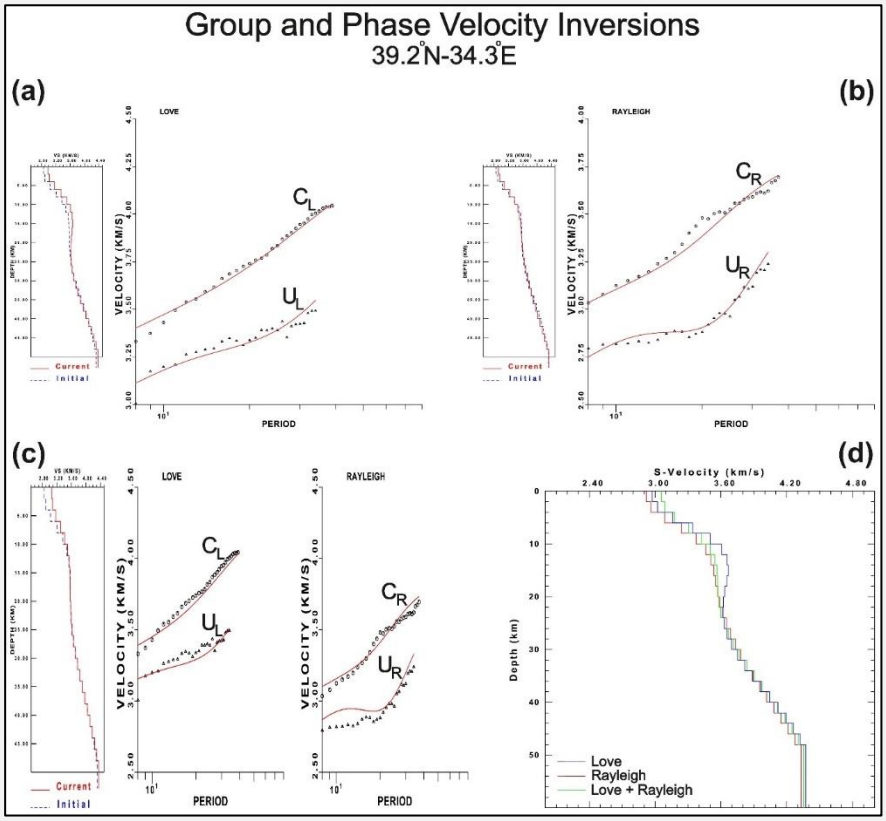

Figure 17. Inverted shear-wave velocity-depth profiles. Phase (C) and group (U) velocity dispersion curves are jointly inverted. Love surface wave inversion (a), Rayleigh surface wave inversion (b), and Love and Rayleigh surface waves inverted jointly (c) are illustrated. The panel (d) displays all three velocity-depth profiles together. The relevant geographic location (39.2°N, 34.3°E) is given in the upper row.

DISCUSSIONS

In geophysical modelling, the general trend is to utilize the multiple data sets (i.e., seismic, gravity, electrical and magnetics) to delineate the underground structure in multi-physics fashion via the joint inversion or imaging (e.g., Gallardo & Meju, 2011). For instance, the joint inversion is followed in studying the surface waves and receiver functions for the structural inversion where the joint inversion is shown to delineate the subsurface velocity discontinuities better compared to these data sets inverted alone (Çakır & Erduran, 2003; Wu et al., 2022). In this respect, the current findings have the great potential to be jointly evaluated with the receiver functions as a future work (Ammon, 1991; Çakır, 2009; Erduran et al., 2022).

Joint Inversion of Receiver Functions and Dispersion Curves

In Fig. 18, we briefly show how the joint inversion made of surface waves (SW) and receiver functions (RF) works. The surface wave information in terms of the phase and group velocity dispersion curves is acquired from the surface tomography such as currently performed. Fig 18a displays the Central Anatolian map along with the 0.05° x 0.05° – sized grid utilized for the surface tomography, which provides the individual dispersion curves (Figs. 17 and E.1) required for the joint inversion of SW and RF. The representative ray paths and waveforms for the surface waves are presented in Figs. 18b and 18d. In actual applications, numerous such ray paths and the corresponding waveforms are considered in a tomographic method for which the current study constitutes one good example. The receiver functions computed from teleseismic P and S wave arrivals are effective to study the crust and upper mantle velocity structure beneath a seismic station for which the representative ray paths and RF waveforms are illustrated in Figs. 18c and 18e. Both SW and RF propagating in geologically similar structure could be

jointly employed to resolve the relevant geological structure. The SW is more effective to resolve the average velocity structure while the RF performs better on the velocity discontinuities (Julià et al., 2000).

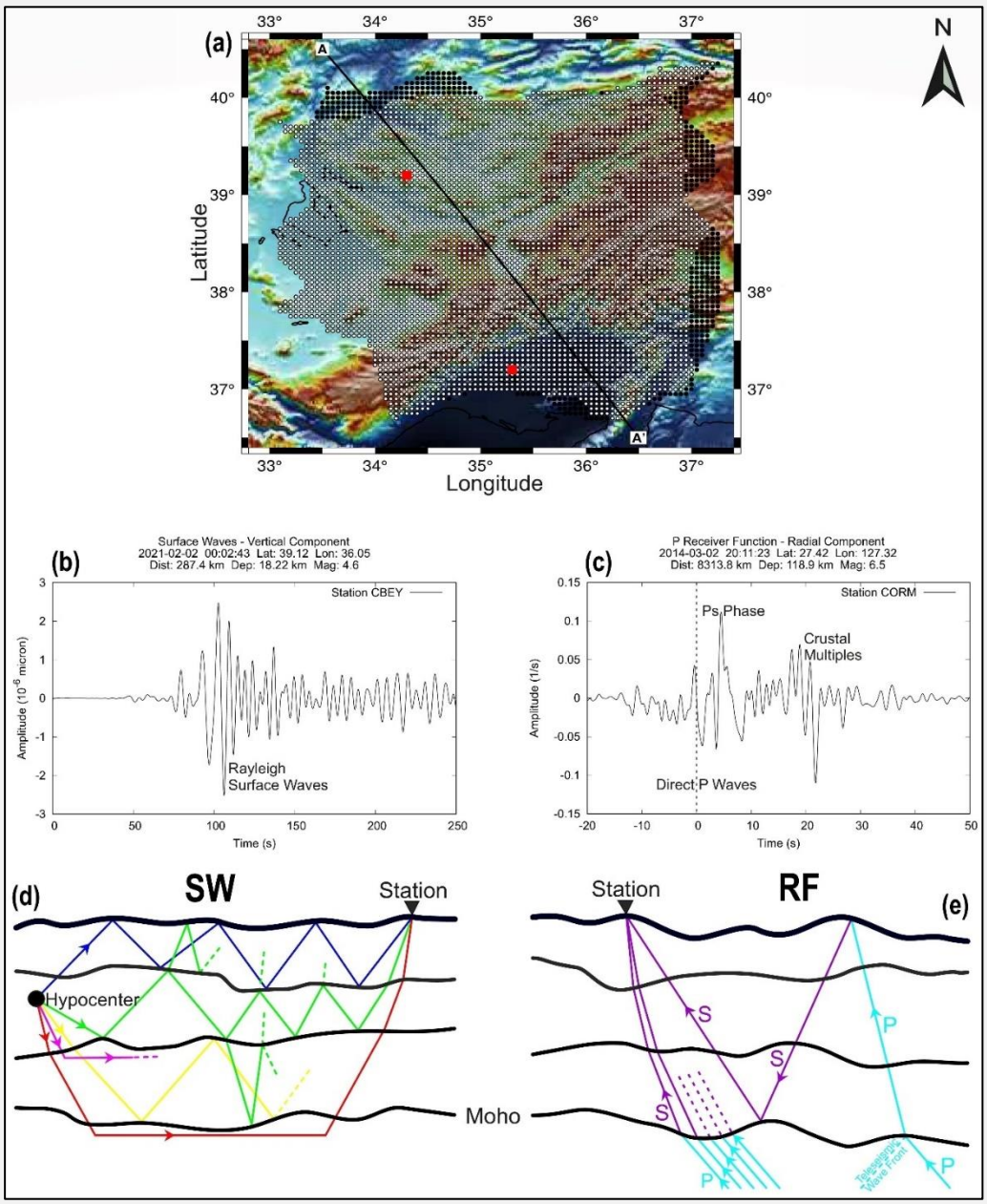

Figure 18. The Central Anatolian map (a). Profile A-A', read squares to indicate the inversion locations utilized in Figs. 17 and E.1 and tomography grid points are superimposed on the map. Rayleigh surface wave (b) recorded at station CBEY and representative ray paths (d) for surface waves in the crust are shown to the left. Receiver function (c) computed at station CORM and representative ray paths (e) for receiver function in the crust are shown to the right.

Joint Analysis of Surface Waves and Gravity

The joint analysis of seismic and gravity data is frequently employed to resolve the crust and upper mantle structure (Syracuse et al., 2017; Scarponi et al., 2021). In this respect, the current findings have the great potential to be jointly evaluated with the gravity data as a future work (Silva & Barbosa, 2006; Cai et al., 2018). In Fig. 19, we sketchily show how the 2-D cross-section (Profile A-A' in Fig. 18a) of the subsurface shear-wave velocities obtained from the surface wave tomography could be employed to compute the approximate densities (ρ) for the same depths (Fig. 19c). The following Nafe-Drake curve (Brocher, 2005) is utilized to compute the relating density values (gr/cm^3).

$$\rho = 1.6612V_P - 0.4721V_P^2 + 0.0671V_P^3 - 0.0043V_P^4 + 0.000106V_P^5 \quad (4)$$

where V_P is the compressional-wave velocity computed from the shear-wave velocity V_S via the expression $V_P = \sqrt{3}V_S$. The 2-D density cross-section in Fig. 19c approximately gives the density-depth distribution, which could be employed as starting point for the subsequent gravity inversions (Syracuse et al., 2016) and then could be revised according to the misfit between the observed and the inverted gravity values. The mentioned joint analysis of the seismic and gravity data could be performed in 3-D depending on the availability of data and computational facilities.

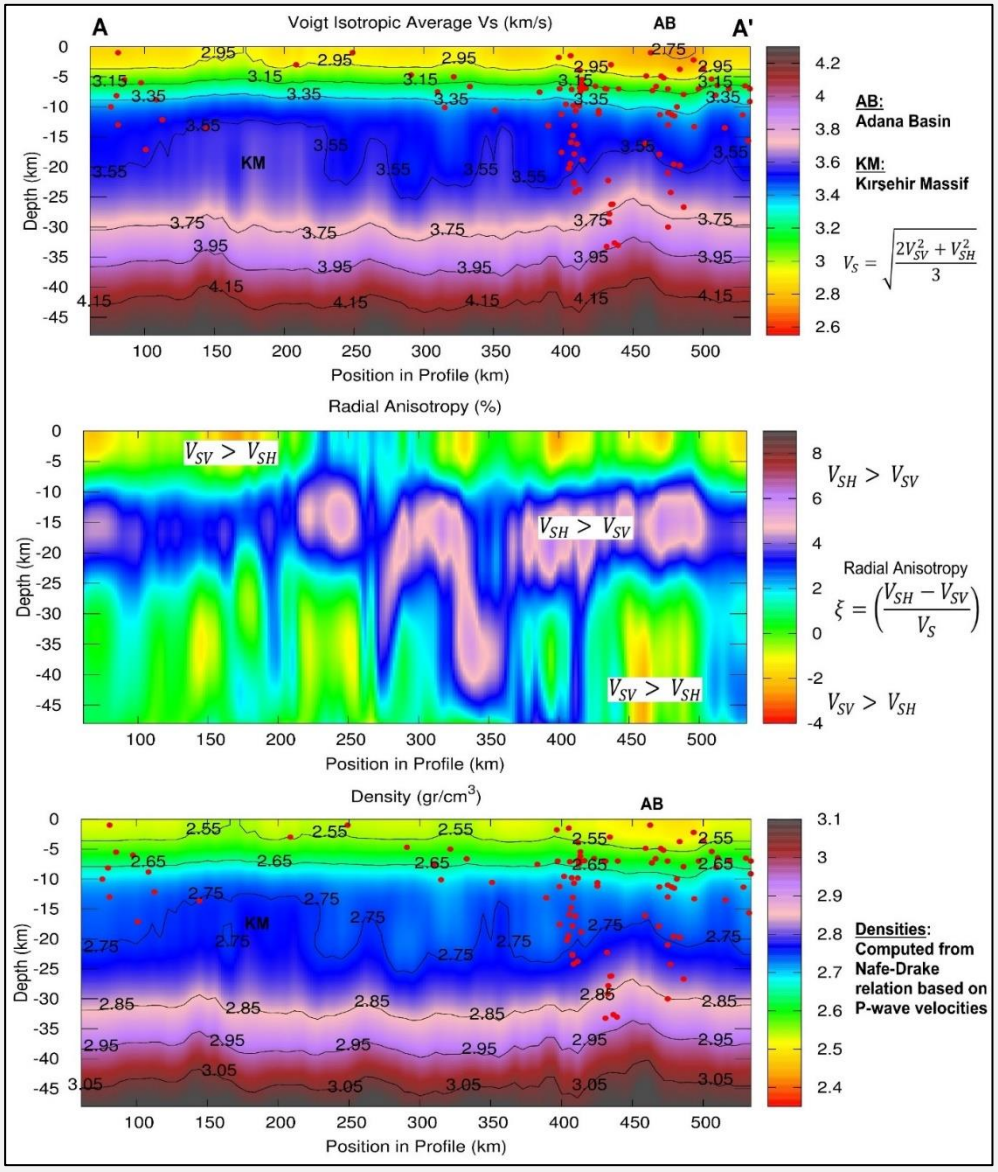

Figure 19. The attained Voigt isotropic average *S*-wave velocities (a) along with the earthquake hypocenters (red color circles), the corresponding radial anisotropy (b) and the densities computed via the Nafe-Drake curve (c) beneath profile A-A'.

Modeling Vertical Transverse Isotropy or Radial Anisotropy

The observed anisotropy (i.e., Love-Rayleigh wave discrepancy) can be modelled using the transverse isotropy with vertical symmetry axis (i.e., radial anisotropy) and the following expressions are used to quantify the relevant anisotropy.

$$V_S^2 = \left(\frac{2V_{SV}^2 + V_{SH}^2}{3}\right) \quad (5)$$

$$\eta = \left(\frac{V_{SH} - V_{SV}}{V_S}\right) \quad (6)$$

where η defines the radial anisotropy (%) and V_S is the Voigt isotropic average shear-wave velocity (km/s). The radial anisotropy (η) is positive when $V_{SH} > V_{SV}$, i.e., the phase velocity surface looks like pumpkin (slow symmetry axis) and negative when $V_{SH} < V_{SV}$, i.e., the phase velocity surface resembles watermelon (fast symmetry axis). The horizontally and vertically polarized shear-wave velocities are given by V_{SH} (km/s) and V_{SV} (km/s), respectively. Both velocities correspond to horizontally propagating shear-waves (for more details, Çakır, 2018 and 2019). Herein the V_{SH} and V_{SV} velocities are acquired from the inversion of Love and Rayleigh surface waves, respectively.

The 2-D tomographic inversions described above provide us with Rayleigh-and-Love group and phase velocities (i.e., four sets of dispersion curves) at these geographical points defined by a 0.05° x 0.05° – sized grid (see Fig. 18a). At each grid point, the Rayleigh group and phase velocity curves are jointly least-squares inverted to obtain the pertinent 1-D shear-wave velocity-depth profile, which gives the V_{SV}. The same is repeated for the Love group and phase velocity curves to attain the V_{SH} and then eqs 5 and 6 are used to compute the relevant depth-dependent radial anisotropy (η) and the Voigt isotropic average shear-wave velocity (V_S). Eventually these 1-D inversions on grid cells of mesh are combined to create pseudo three-dimensional (3-D) images (both η and V_S) of the subsurface.

In Fig. 19, we also show the 2-D cross-section corresponding to the radial anisotropy computed from eq 6 (Fig. 19b). To study the radial anisotropy is helpful to outline the geological fabric as well as deformations caused by tectonic and geodynamic processes (Anderson, 1989). In general, lattice-preferred orientation (LPO) and shape-preferred orientation (SPO) are two mechanisms to cause the radial anisotropy in the Earth. Considering the crustal depth range, the LPO is anisotropy resulting from mineral alignment due to deformations associated with faults and shear zones. The SPO may result from periodic alignment of structures such as networks of cracks and fractures due to the regional stress field near the surface and horizontal bedding structures such as sills due to the deeper magmatic activity (Acevedo et al., 2022).

The current Rayleigh and Love surface wave dispersion curves (group and phase velocities) show discrepancy, i.e., an isotropic model cannot fit all four dispersion curves simultaneously (see Figs. 17 and E.1). The vertical transverse isotropy – VTI is generally applied to resolve the issue of dispersion curve discrepancy, i.e., all four dispersion curves are concurrently fit by a VTI model. The VTI modeling of dispersion curves at a particular location as well as the 2-D cross sections of the radial anisotropy are our next goals to achieve in follow up studies for the Central Anatolian region.

CONCLUSION

The studied (or test) region (i.e., Central Anatolia) taking place above the northward subducting African slab has complex tectonic history manifested by broad fault and suture zones, volcanic intrusions and eruptions, exhumed massifs and wide sedimentary basins. This region is densely covered by broadband seismograph and accelerograph stations. We utilize the local and regional Rayleigh and Love surface waves recorded at these seismic stations to test the proposed method for the effective selection of group and phase velocity dispersion curves. The proposed method has the potential to be used for tomographic investigation of the crust and uppermost mantle velocity structure beneath a region under consideration.

We were able to implement the proposed selection method (particularly second stage) because of the dense seismographic station coverage of the studied region, which is also supported by broader surface waves arrival azimuths. However, the number of surface waves (from particularly regional distances) with arrival azimuths around the north and south is relatively smaller, which we try to alleviate it by adding the local and near field earthquakes from these azimuths into our data set.

ACKNOWLEDGEMENTS

We would like to thank the anonymous reviewers for critically reviewing the manuscript. KOERI (Kandilli Observatory and Earthquake Research Institute) and AFAD (Turkish Disaster and Emergency Management Presidency) are thankfully recognized for providing the seismograms. We gratefully acknowledge the use of Generic Mapping Tool (GMT – Wessel et al., 2013) in several figure illustrations.

REFERENCES

Abgarmi, B., Delph, J. R., Ozacar, A. A., Beck, S. L., Zandt, G., Sandvol, E., Turkelli, N., & Biryol, C.B. (2017). Structure of the crust and African slab beneath the central Anatolian plateau from receiver functions: New insights on isostatic compensation and slab dynamics. *Geosphere, 13*(6), 1774-1787. https://doi.org/10.1130/GES01509.1

Acevedo, J., Fernández-Viejo, G., Llana-Fúnez, S., López-Fernández, C., Olona, J., & Pérez-Millán, D. (2022). Radial anisotropy and S-wave velocity depict the internal to external zone transition within the Variscan orogen (NW Iberia). *Solid Earth, 13*(3), 659–679. https://doi.org/10.5194/se-13-659-2022

AFAD. (2023). *The Turkish Disaster and Emergency Management Presidency*. https://deprem.afad.gov.tr/home-page. Last visited 24.07.2023

Agius, M. R., & Lebedev, S. (2014). Shear-velocity structure, radial anisotropy and dynamics of the Tibetan crust. *Geophysical Journal International, 199*(3), 1395-1415. https://doi.org/10.1093/gji/ggu326

Ammon, C. J. (1991). The isolation of receiver effects from teleseismic P waveforms. *Bulletin of the Seismological Society of America, 81*(6), 2504–2510. https://doi.org/10.1785/BSSA0810062504

Anderson, D. L. (1989). *Theory of the Earth*. Boston, MA: Blackwell Scientific Publications.

Arcasoy, A. (2001). *A new method for detecting the alignments from point-like features: an application to the volcanic cones of Cappadocian Volcanic Province*. PhD thesis, Middle East Technical University, Ankara.

Aydar, E., Diker, C., Ulusoy, I., & Şen, E. (2021). Volcanic unrest possibilities in response to recent Obruk seismic swarm on and around Hasandağ stratovolcano (Central Anatolia, Turkey). *Comptes Rendus. Géoscience, 353*, 1-18. https://doi.org/10.5802/crgeos.46

Aydin, F. (2008). Contrasting complexities in the evolution of calc-alkaline and alkaline melts of the Nigde volcanic rocks, Turkey: textural, mineral chemical and geochemical evidence. *European Journal of Mineralogy, 20*(1), 101-118. https://doi.org/10.1127/0935-1221/2008/0020-1784

Barka, A. A., & Kadinsky-Cade, K. (1988). Strike-slip fault geometry in Turkey and its influence on earthquake activity. *Tectonics, 7*(1), 663- 684. https://doi.org/10.1029/TC007i003p00663

Barmin, M., Ritzwoller, M., Levshin, A. (2001). A fast and reliable method for surface wave tomography. *Pure and Applied Geophysics, 158*, 1351-1375. https://doi.org/10.1007/PL00001225

Bartol, J., & Govers, R. (2014). A single cause for uplift of the Central and Eastern Anatolian plateau? *Tectonophysics, 637*, 116-136. https://doi.org/10.1016/j.tecto.2014.10.002

Berteussen, K. A. (1977). Moho depth determinations based on spectral analysis of NORSAR long period P waves. *Physics of the Earth and Planetary Interiors, 15*(1), 13–27. https://doi.org/10.1016/0031-9201(77)90006-1

Bozkurt, E. (2001). Neotectonics of Turkey-a synthesis. *Geodinamica Acta, 14(1-3)*, 3–30. https://doi.org/10.1016/S0985-3111(01)01066-X

Boztuğ, D., Jonckheere, R. C., Heizler, M., Ratschbacher, L., Harlavan, Y., & Tichomirova, M. (2009). Timing of post-obduction granitoids from intrusion through cooling to exhumation in central Anatolia, Turkey. *Tectonophysics, 473*(1-2), 223-233. https://doi.org/10.1016/j.tecto.2008.05.035

Boztuğ, D., Temiz, H., Jonckheere, R., & Ratschbacher, L. (2008). Punctuated exhumation and Foreland Basin formation and infilling in (circum)-Central Anatolia (Turkey) associated with the neo-tethyan closure. *Turkish Journal of Earth Sciences, 17*(4), 673-684.

Brocher, T. (2005). Empirical Relations between Elastic Wavespeeds and Density in the Earth's Crust. *Bulletin of the Seismological Society of America, 95*(6), 2081-2092. https://doi.org/10.1785/0120050077

Cai, H., Xiong, B., & Zhu, Y. (2018). 3D modeling and inversion of gravity data in exploration scale. In Zouaghi, T. (Ed.), *Gravity - Geoscience Applications, Industrial Technology and Quantum Aspect*. InTech (pp 401-406. https://doi.org/10.5772/intechopen.70961

Çakır, Ö. (2006). The multilevel fast multipole method for forward modelling the multiply scattered seismic surface waves. *Geophysical Journal International, 167*(2), 663–678. https://doi.org/10.1111/j.1365-246X.2006.02928.x

Çakır, Ö. (2009). Forward modelling the multiply scattered 2.5-D teleseismic P waves accelerated by the multilevel fast multipole method. *Geophysical Journal International, 176*(2), 505–517. https://doi.org/10.1111/j.1365-246X.2008.03960.x

Çakır, Ö. (2018). Seismic crust structure beneath the Aegean region in southwest Turkey from radial anisotropic inversion of Rayleigh and Love surface waves. *Acta Geophysica, 66*, 1303–1340. https://doi.org/10.1007/s11600-018-0223-1

Çakır, Ö. (2019). Love and Rayleigh waves inverted for vertical transverse isotropic crust structure beneath the Biga Peninsula and the surrounding area in NW Turkey. *Geophysical Journal International, 216*(3), 2081–2105. https://doi.org/10.1093/gji/ggy538

Çakır, Ö. (2021). Transverse Isotropic Crust Structure Beneath the Northwest and Central North Anatolia Revealed by Seismic Surface Waves Propagation. *Malaysian Journal of Geosciences, 5*(2), 41–50. https://doi.org/10.26480/mjg.02.2021.41.50

Çakır, Ö., & Erduran, M. (2001). Effect of earth structure and source time function on inversion of single station regional surface waves for rupture mechanism and focal depth. *Journal of the Balkan Geophysical Society, 4*(4), 69-90.

Çakır, Ö., & Erduran, M. (2003). Determination of crustal structure from joint inversion of receiver function and surface wave information (in Turkish). *Yerbilimleri, 27*, 29–46.

Çakır, Ö., Erduran, M., & Livaoğlu, S. (2000). The effect of the initial earthquake phase shift on the inversion of regional surface wave recordings for the estimation of crustal structure. *Journal of the Balkan Geophysical Society, 3*(2), 20-36.

Chen, H., Li, Z., Luo, Z., Ojo, A.O., Xie, J., Bao, F., Wang, L., & Tu, G. (2021). Crust and upper mantle structure of the South China Sea and adjacent areas from the joint inversion of ambient noise and earthquake surface wave dispersions. *Geochemistry Geophysics Geosystems, 22*(3), e2020GC009356. https://doi.org/10.1029/2020GC009356

Chen, H., Ni, S., Chu, R., Chong, J., Liu, Z., & Zhu, L. (2018). Influence of the off-great-circle propagation of Rayleigh waves on event-based surface wave tomography in Northeast China. *Geophysical Journal International, 214*(2), 1105-1124. https://doi.org/10.1093/gji/ggy185

Dal Moro, G., & Ferigo, F. (2011). Joint analysis of Rayleigh and Love wave dispersion for near-surface studies: issues, criteria and improvements. *Journal of Applied Geophysics, 75*(3), 573-589. https://doi.org/10.1016/j.jappgeo.2011.09.008

Demirsıkan, İ. H., Şahin, Ş., & Öksüm, Ö. (2019). Determination of seismic P and S wave velocity structure of crust in central Anatolia, Pamukkale University. *Journal of Engineering Sciences, 25*(6), 775-784 (in Turkish). https://doi.org/10.5505/pajes.2018.45548

Dewey, J. F., & Şengör, A. M. C. (1979). Aegean and surrounding regions: complex multiplate and continuum tectonics in a convergent zone. *Geological Society of America Bulletin, 90*(1), 84–92, https://doi.org/10.1130/0016-7606(1979)90<84:AASRCM>2.0.CO;2

Dewey, J. F., Helman, M. L., Turco, E., Hutton, D. H. W., & Knott, S. D. (1989). Kinematics of the western Mediterranean. In Coward M. P., Dietrich, D., & Park, R. G. (Eds.), *Alpine Tectonics, Geological Society Special Publication no. 45*. Geological Society, London (pp. 265-283).

Dilek, Y., & Altunkaynak, Ş. (2007). Cenozoic crustal evolution and mantle dynamics of post collisional magmatism in Western Anatolia. *International Geology Review, 49*(5), 431-453. https://doi.org/10.2747/0020-6814.49.5.431

Dilek, Y., Altunkaynak, Ş., & Öner, Z. (2009). Syn-extensional granitoids in the Menderes core complex and the late Cenozoic extensional tectonics of the Aegean province. In Ring, U., & Wernicke, B. (Eds.), *Extending a continent: architecture, Rheology and Heat Budget. Geological Society, London, Special Publications*, 197-223. https://doi.org/10.1144/SP321.10

Dirik, K., & Goncuoglu, M. C. (1996). Neotectonic characteristics of Central Anatolia. *International Geology Review, 38*(9), 807-817. https://doi.org/10.1080/00206819709465363

Duman, T. Y., Çan, T., Emre, Ö., Kadirioğlu, F. T., Başarır-Baştürk, N., Kılıç, T., Arslan, S., Özalp, S., Kartal, R. F., Kalafat, D., Karakaya, F., Eroğlu-Azak, T., Özel, N.M., Ergintav, S., Akkar, S., Altınok, Y., Tekin, S., Cingöz, A., & Kurt, A. I. (2018). Seismotectonics database of Turkey. *Bulletin of Earthquake Engineering, 16*, 3277-3316. https://doi.org/10.1007/s10518-016-9965-9

Erduran, M., Oreshin, S., Vinnik, L., Çakır, Ö., & Makeyeva, L. (2022). Mantle lithosphere, asthenosphere and transition zone beneath Eastern Anatolia. *Journal of Seismology, 26*, 265–281. https://doi.org/10.1007/s10950-022-10074-z

Faccenna, C., Becker, T. W., Auer, L., Billi, A., Boschi, L., Brun, J. P., Capitanio, F. A., Funiciello, F., Horvath, F., Jolivet, L., Piromallo, C., Royden, L., Rossetti, F., & Serpelloni, E. (2014). Mantle dynamics in the Mediterranean. *Reviews of Geophysics, 52*(3), 283–332, https://doi.org/10.1002/2013RG000444

Fang, H., Zhang, H., Yao, H., Allam, D., Zigone, D., Ben-Zion, Y., Thurber, C., & van der Hilst, R. D. (2016). A new three-dimensional joint inversion algorithm of body-wave and surface-wave data and its application to the Southern California Plate Boundary Region. *Journal of Geophysical Research, 121*(5), 3557-3569. https://doi.org/10.1002/2015JB012702

Gallardo, L. A., & Meju, M. A. (2011). Structure-coupled multiphysics imaging in geophysical sciences. *Reviews of Geophysics, 49*(1), RG1003. https://doi.org/10.1029/2010RG000330

Güçtekin, A., & Köprübaşi, N. (2009). Geochemical characteristics of mafic and intermediate volcanic rocks from the Hasandağ and Erciyes volcanoes (Central Anatolia, Turkey). *Turkish Journal of Earth Sciences, 18*(1), 1-27. https://doi.org/10.3906/yer-0806-2

Herrmann, R. B. (2017*). Computer Programs in Seismology.* Open files. http://www.eas.slu.edu/People/RBHerrmann/CPS330.html. (Accessed March 2017)

Higgins, M., Schoenbohm, L. M., Brocard, G., Kaymakci, N., Gosse, J. C., & Cosca, M.A. (2015). New kinematic and geochronologic evidence for the Quaternary evolution of the Central Anatolian fault zone (CAFZ). *Tectonics, 34*(10), 2118–2141. https://doi.org/10.1002/2015TC003864

Julià, J., Ammon, C. J., Herrmann, R. B., & Correig, A. M. (2000). Joint inversion of receiver function and surface wave dispersion observations. *Geophysical Journal International, 143*(1), 99–112. https://doi.org/10.1046/j.1365-246x.2000.00217.x

Karaoğlu, Ö., Selçuk, A. S., & Gudmundsson, A. (2017). Tectonic controls on the Karlıova triple junction (Turkey): implications for tectonic inversion and the initiation of volcanism. *Tectonophysics, 694*, 368-384. https://doi.org/10.1016/j.tecto.2016.11.018

Kästle, E. D., El-Sharkawy, A., Boschi, L., Meier, T., Rosenberg, C., Bellahsen, N., Cristiano, L., & Weidle, C. (2018). Surface wave tomography of the Alps using ambient-noise and earthquake phase velocity measurements. *Journal of Geophysical Research, 123*(2), 1770-1792. https://doi.org/10.1002/2017JB014698

Keller, J. (1974). Quaternary maar volcanism near Karapinar in Central Anatolia. *Bulletin Volcanologique, 36*, 378–396. https://doi.org/10.1007/BF02599413

Kennett, B. L. N., & Engdahl, E. R. (1991). Traveltimes for global earthquake location and phase identification. *Geophysical Journal International, 105*(2), 429–465. https://doi.org/10.1111/j.1365-246X.1991.tb06724.x

Koçyiğit, A., & Beyhan, A. (1998). A new intracontinental transcurrent structure: the Central Anatolian Fault Zone, Turkey. *Tectonophysics, 284*(3-4), 317-336. https://doi.org/10.1016/S0040-1951(97)00176-5

KOERI. (2023). *Kandilli Observatory and Earthquake Research Institute*. http://www.koeri.boun.edu.tr/new/. Last visited 24.07.2023

Korkmaz, G. G., Kurt, H., Asan, K., & Leybourne, M. (2022). Ar-Ar Geochronology and Sr-Nd-Pb-O Isotopic Systematics of the Post-collisional Volcanic Rocks from the Karapınar-Karacadağ Area (Central Anatolia, Turkey): An Alternative Model for Orogenic Geochemical Signature in Sodic Alkali Basalts. *Journal of Geosciences, 67*(1), 53-69. https://doi.org/10.3190/jgeosci.343

Krystopowicz, N. J., Schoenbohm, L. M., Rimando, J., Brocard, G., & Rojay, B. (2020). Tectonic geomorphology and Plio-Quaternary structural evolution of the Tuzgölü fault zone, Turkey: Implications for deformation in the interior of the Central Anatolian Plateau. *Geosphere, 16*(5), 1107-1124. https://doi.org/10.1130/GES02175.1

Li, L., Li, A., Murphy, M. A., & Fu, Y. V. (2016). Radial anisotropy beneath northeast Tibet, implications for lithosphere deformation at a restraining bend in the Kunlun fault and its vicinity. *Geochemistry, Geophysics, Geosystems, 17*(9), 3674-3690. https://doi.org/10.1002/2016GC006366

Lines, L. R., & Treitel, S. (1984). A review of least-squares inversion and its application to geophysical problems. *Geophysical Prospecting, 32*(2), 159-186. https://doi.org/10.1111/j.1365-2478.1984.tb00726.x

Magrini, F., Lauro, S., Kästle, E., & Boschi, L. (2022). Surface-wave tomography using SeisLib: a Python package for multi-scale seismic imaging. *Geophysical Journal International, 231*(2), 1011-1030. https://doi.org/10.1093/gji/ggac236

Movaghari, R., JavanDoloei, G., Yang, Y., Tatar, M., & Sadidkhouy, A. (2021). Crustal radial anisotropy of the Iran Plateau inferred from ambient noise tomography. *Journal of Geophysical Research: Solid Earth, 126*(4), e2020JB020236. https://doi.org/10.1029/2020JB020236

Özsayın, E., Çiner, A., Rojay, B., Dirik, K., Melnick, D., Fernandez-Blanco, D., Bertotti, G., Schildgen, T. F., Garcin, Y., Strecker, M. R., & Sudo, M. (2013). Plio-Quaternary extensional tectonics of the Central Anatolian Plateau: a case study from the Tuzgölü Basin, Turkey. *Turkish Journal of Earth Sciences, 22*(5), 691–714. https://doi.org/10.3906/yer-1210-5

Rawlinson, N. (2005). *FMST: Fast marching surface tomography package*. Research School of Earth Science, Australian National University, Canberra.

Rawlinson, N., & Sambridge, M. (2003). Seismic traveltime tomography of the crust and lithosphere. *Advances in Geophysics, 46*, 81–198. https://doi.org/10.1016/S0065-2687(03)46002-0

Rawlinson, N., & Sambridge, M. (2005). The fast marching method. An effective tool for tomographic imaging and tracking multiple phases in complex layered media. *Exploration Geophysics, 36*(4), 341–350. https://doi.org/10.1071/EG05341

SAGE. (2023). *Seismological Facility for the Advancement of Geoscience*. https://ds.iris.edu/ds/. Last visited 15.08.2023

Salaün, G., Pedersen, H., Paul, A., Farra, V., Karabulut, H., Hatzfeld, D., Childs, D.M., Pequegnat, C., & the SIMBAAD. (2012). Team High-resolution surface wave tomography beneath the Aegean-Anatolia region: constraints on upper mantle structure. *Geophysical Journal International, 190*(1), 406-420. https://doi.org/10.1111/j.1365-246X.2012.05483.x

Sarjan, A. F. N., Zulfakriza, Z., Nugraha, A. D., Rosalia, S., Wei, S., Widiyantoro, S., Cummins, P. R., Muzli, M., Sahara, D. P., Puspito, N. T., Priyono, A., & Afif, H. (2021). Delineation of upper crustal structure beneath the Island of Lombok, Indonesia, using ambient seismic noise tomography. *Frontiers in Earth Science, 9*, 560428. https://doi.org/10.3389/feart.2021.560428

Saygin, E., & Kennett, B. L. N. (2010). Ambient seismic noise tomography of Australian continent. *Tectonophysics, 481*(1-4), 116-125. https://doi.org/10.1016/j.tecto.2008.11.013

Scarponi, M., Hetényi, G., Plomerová, J., Solarino, S., Baron, L., & Petri, B. (2021). Joint Seismic and Gravity Data Inversion to Image Intra-Crustal Structures: The Ivrea Geophysical Body Along the Val Sesia Profile (Piedmont, Italy). *Frontiers in Earth Science, 9*, 671412. https://doi.org/10.3389/feart.2021.671412

Schildgen, T. F., Yildirim, C., Cosentino, D., & Strecker, M. R. (2014). Linking slab break-off, Hellenic trench retreat, and uplift of the central and eastern Anatolian plateaus. *Earth-Science Reviews, 128*, 147–168. https://doi.org/10.1016/j.earscirev.2013.11.006

Şengör, A. M. C., & Yılmaz. Y. (1981). Tethyan evolution of Turkey: a plate tectonic approach. *Tectonophysics, 75*(3-4), 181–241. https://doi.org/10.1016/0040-1951(81)90275-4

Sethian, J. A., & Popovici, A. M. (1999). 3-D traveltime computation using the fast marching method. *Geophysics, 64*(2), 516-523. https://doi.org/10.1190/1.1444558

Silva, J. B. C., & Barbosa, V. C. F. (2006). Interactive gravity inversion. *Geophysics, 71*(1), J1–J9. https://doi.org/10.1190/1.2168010

Styron, R., & Pagani, M. (2020). The GEM Global Active Faults Database. *Earthquake Spectra, 36*(S1), 160–180. https://doi.org/10.1177/8755293020944182

Syracuse, E. M., Maceira, M., Prieto, G. A., Zhang, H., & Ammon, C. J. (2016). Multiple plates subducting beneath Colombia, as illuminated by seismicity and velocity from the joint inversion of seismic and gravity data. *Earth and Planetary Science Letters, 444*, 139-149. https://doi.org/10.1016/j.epsl.2016.03.050

Syracuse, E. M., Zhang, H., & Maceira, M. (2017). Joint inversion of seismic and gravity data for imaging seismic velocity structure of the crust and upper mantle beneath Utah, United States. *Tectonophysics, 718*, 105-117. https://doi.org/10.1016/j.tecto.2017.07.005

Tarantola, A. (1987). *Inverse problem theory.* Elsevier Science Company Inc., Amsterdam (pp 187–255).

Tohti, M., Liu, J., Xiao, W., Wang, Y., Di, Q., & Zhou, K. (2022). Full-wave-form inversion of surface waves based on instantaneous-phase coherency. *Near Surface Geophysics, 20*(5), 494–506. https://doi.org/10.1002/nsg.12229

Toprak, V. (1998). Vent distribution and its relation to regional tectonics, Cappadocian Volcanics, Turkey. *Journal of Volcanology and Geothermal Research, 85*(1-4), 55–67. https://doi.org/10.1016/S0377-0273(98)00049-3

USGS. (2023*). United States Geological Survey*. https://www.usgs.gov/. Last visited 24.07.2023

Uslular, G., & Gençalioğlu-Kuşcu, G. (2019). Geochemical Characteristics of Anatolian Basalts: Comment on "Neogene Uplift and Magmatism of Anatolia: Insights from Drainage Analysis and Basaltic Geochemistry" by McNab Et Al.. *Geochemistry, Geophysics, Geosystems, 20*(1), 530-541. https://doi.org/10.1029/2018GC007533

Uslular, G., Gençalioğlu-Kuşcu, G., & Arcasoy, A. (2015). Size-distribution of scoria cones within the Eğrikuyu monogenetic field (Central Anatolia, Turkey). *Journal of Volcanology and Geothermal Research, 301*, 56-65. https://doi.org/10.1016/j.jvolgeores.2015.05.006

Uslular, G., Le Corvec, N., Mazzarini, F., Legrand, D., & Gençalioğlu-Kuşcu, G. (2021). Morphological and multivariate statistical analysis of quaternary monogenetic vents in the Central Anatolian Volcanic Province (Turkey): Implications for the volcano-tectonic evolution. *Journal of Volcanology and Geothermal Research, 416*, 107280. https://doi.org/10.1016/j.jvolgeores.2021.107280

Wang, Y., & Pavlis, G. L. (2016). Generalized iterative deconvolution for receiver function estimation. *Geophysical Journal International, 204(*2), 1086–1099. https://doi.org/10.1093/gji/ggv503

Wessel, P., Smith, W. H. F., Scharroo, R., Luis, J. F., & Wobbe, F. (2013). Generic mapping tools: improved version released. *Eos, Transactions American Geophysical Union, 94*(45), 409–410. https://doi.org/10.1002/2013EO450001

Wu, J., Liu, Y., Zhong, S., Wang, W., Cai, Y., Wang, W., & Liu, J. (2022). Lithospheric structure beneath Ordos Block and surrounding areas from joint inversion of receiver function and surface wave dispersion. *Science China Earth Sciences, 65*, 1399–1413. https://doi.org/10.1007/s11430-021-9895-0

Yıldırım, C. (2014). Relative tectonic activity assessment of the Tuz Gölü fault zone, central Anatolia, Turkey. *Tectonophysics, 630*, 183-192. https://doi.org/10.1016/j.tecto.2014.05.023

Zhang, X., Zheng, Y., & Curtis, A. (2023). Surface wave dispersion inversion using an energy likelihood function. *Geophysical Journal International, 232*(1), 523–536. https://doi.org/10.1093/gji/ggac331

Zhou, B., Greenhalgh, S. A., & Sinadinovski, C. (1992). Iterative algorithm for the damped minimum norm, least squares and constrained problem in seismic tomography. *Exploration Geophysics, 23*(3), 497–505. https://doi.org/10.1071/EG992497

Zhou, Z., Wiens, D. A., Shen, W., Aster, R. C., Nyblade, A., & Wilson, T. J. (2022). Radial anisotropy and sediment thickness of West and Central Antarctica estimated from Rayleigh and Love wave velocities. *Journal of Geophysical Research: Solid Earth, 127*(3), e2021JB022857. https://doi.org/10.1029/2021JB022857

Zhu, R., Zhao, P., & Zhao, L. (2022). Tectonic evolution and geodynamics of the Neo-Tethys Ocean. *Science China Earth Science, 65*, 1–24. https://doi.org/10.1007/s11430-021-9845-7

Appendix A: Single-Station Group Velocity Dispersion Curve Selection

The group velocity procedure described in this appendix is separately applied to single-station Rayleigh and Love surface wave observations at each station. In Fig. A.1, we show some curves utilized in the selection of the observed group velocity dispersion curves. The group velocities with these values above the upper bonds applied differently to the Rayleigh (R - green color in left panel) and Love (L - brown color in left panel) surface waves are discarded from the data set. To compare with the current group velocities, the fundamental mode group velocity dispersion curves of Rayleigh (purple color in left panel) and Love (blue color in left panel) surface waves corresponding to the global IASP91 model (Kennett & Engdahl, 1991) are also shown. In addition, the gradient (G) change in the group velocity, i.e., $G = dV/dT$ where V is group velocity (km/s) and T is period (s), on a dispersion curve is restricted. The $G = dV/dT$ value may be positive or negative. A positive value is restricted to be less than the value defined by the upward gradient curve where the Rayleigh (r) surface wave is represented by the cyan color curve (Gru) and the Love (l) surface waves by the pink color curve (Glu). A negative value is restricted to be greater than the value defined by the downward gradient curve where the Rayleigh surface wave is represented by the orange color curve (Grd) and the Love surface waves by the magenta color curve (Gld). In other words, the $Gr = dV/dT$ value computed for the Rayleigh group velocity should satisfy the condition $Grd \leq Gr \leq Gru$. The same is also true for the Love group velocities, i.e., $Gl = dV/dT$ and $Gld \leq Gl \leq Glu$. This restriction helps us select smooth and continuous dispersion curves where the discontinuities and jumps on the observed curves are effectively avoided.

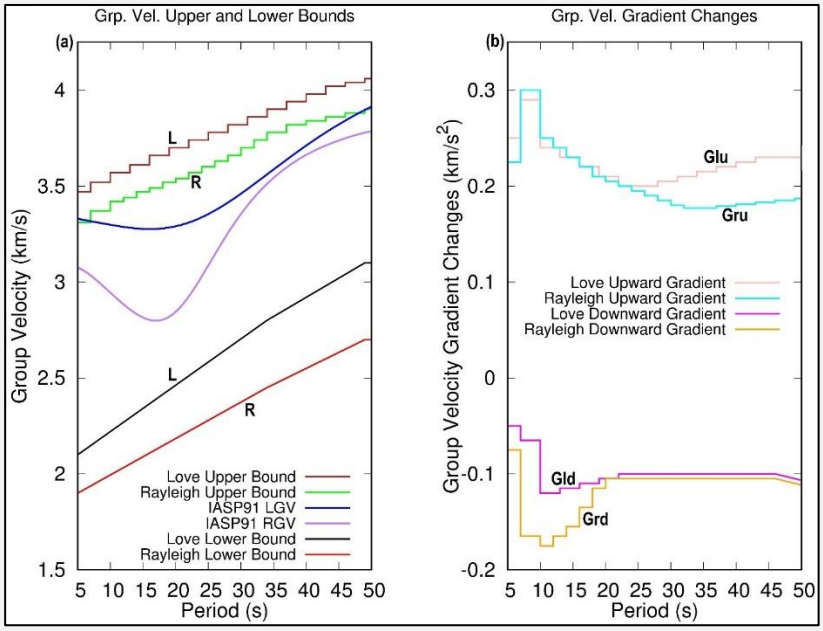

Figure A.1. Group velocity upper and lower bonds along with the fundamental mode Rayleigh (R) and Love (L) surface wave group velocity (GV) dispersion curves corresponding to the IASP91 model (Kennett & Engdahl, 1991) are shown in the left panel. Upward and downward gradient changes along each group velocity curve is restricted according to the curves given in the right panel.

We did not actually apply any lower bonds to the observed dispersion curves, but the restrictions implemented through the curves for the gradient (G) changes in the right panel indirectly yield the lower bonds approximately shown by the red (Rayleigh) and black (Love) color curves in the left panel. In the selection procedure implemented through the conditions described in Fig. A.1, the minimum length of the group velocity curve measured with respect to surface wave period is initially taken 5 s. At the final step, these dispersion curves shorter than 8 s are discarded from the data set. The shorter length (i.e., < 8 s) dispersion curves occasionally caused inversion problems due to the underdetermined inversion system (i.e., see Appendix B), which is alleviated by increasing the dispersion curve length to at least 8-s. The continuum of each curve in Fig. A.1 is determined after several trial-and-error experiments, which may need some minor/major revisions if it is applied to a different region.

In Fig. A.2, we display examples of Love (Figs. A.2a and A.2b) and Rayleigh (Figs. A.2c and A.2d) surface waves where both MFT diagrams (Figs. A.2b and A.2d) obtained for station ALIN fail to show continuous maximums on the group velocity–period profile surfaces. The modal spectral amplitudes show several overlapping peaks where the fundamental mode energy is not visibly isolated. There does not exist surface wave generation as shown by the waveforms attached to the MFT diagrams on the right (compare to Figs. 5b and 5d). Perhaps there was some timing error (i.e., clock accuracy problem) occurring on this station or the noise conditions around the station location were severe masking the surface wave signal. The automatic group velocity selection system currently implemented on the base of the MFT diagrams marked this data as unusable.

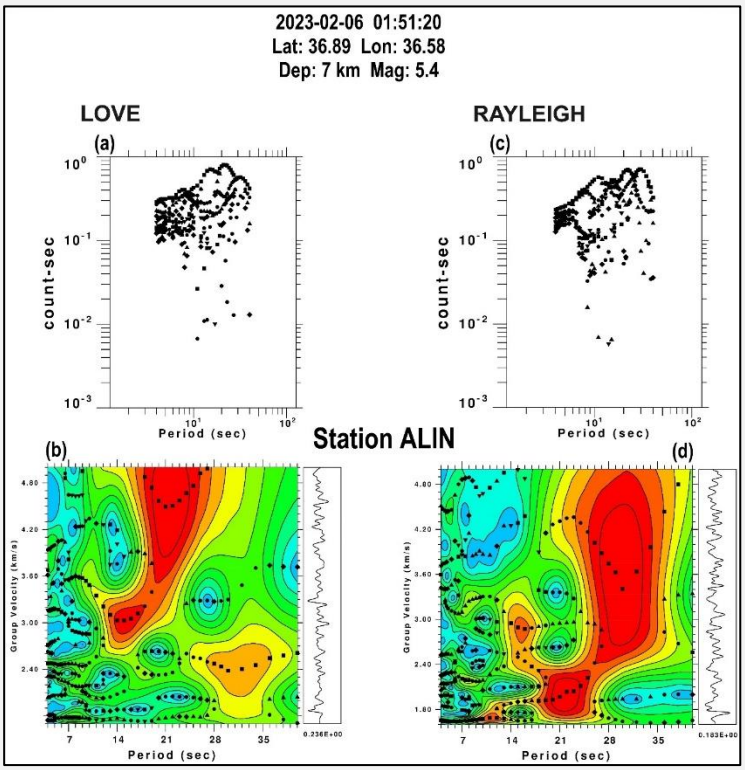

Figure A.2. Failed examples of the MFT analysis applied to the observed single-station Love (panels a and b) and Rayleigh (panels c and d) surface waves are shown for station ALIN.

Appendix B: Two-Station Phase and Group Velocity Dispersion Curve Selection

The phase and group velocity procedure illustrated in this appendix is separately applied to two-station Rayleigh and Love surface wave observations between each pair of station. To measure the level of dispersion misfit after an inversion, we utilize an error value, which is computed from $E = (\sum_{i=1}^{N} |v_i^{sel} - v_i^{inv}|)^{1/2}/N$ where N is the number of phase and group velocities, v_i^{sel} stands for the selected phase and group velocities and v_i^{inv} represents the inverted phase and group velocities. In the dispersion curve inversion, we employ the least-squares inversion technique (Herrmann, 2017) linearized around an initial model, which is obtained from the inversion of average single-station Rayleigh group velocities presented in Fig. 11c. In the latter inversion, the half-space model with 4.0 km/s shear-wave velocity is employed as the initial model. The inversion is only performed for the shear-wave velocities (V_S) where the compressional-wave velocities (V_P) are computed from $V_P = \sqrt{3}V_S$, i.e., Poisson's ratio is 0.25. The wave propagating medium with 48-km thickness is assumed multi-layered containing 24 layers each with 2-km thickness and located above a half-space. We fix the layer thickness and compute the density from $\rho = 0.32V_P + 0.77$ (Berteussen, 1977). Herein the initial model is always indicated by the blue color dashed line on each illustration of the dispersion inversion. The linearized inversion system is solved in 20 successive steps and each step is regularized using a damping parameter, which is set to 10.0 in the first step and then linearly decreased to 1.0 at the final step. More details regarding the damped least squares technique are provided in the literature (Lines & Treitel, 1984; Zhou et al., 1992; Herrmann, 2017; Çakır, 2018 and 2019).

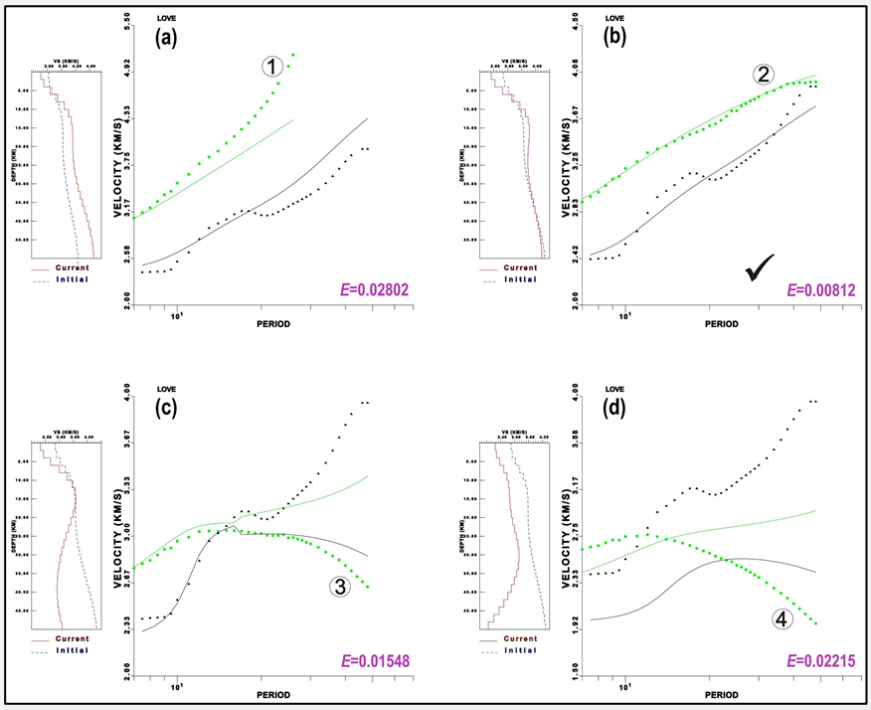

Figure B.1. The two-station selection procedure based on the joint inversion of phase and group velocities is shown for the Love surface waves. The event and station parameters are listed on top. Different phase velocity branches specified by 1, 2, 3 and 4 refer to Fig. 6c. The best solution is indicated by a check mark.

In Fig. B.1, we display the subsequent procedure for the Love surface waves where the group velocity curve (black color symbols) is acquired from the MFT diagram in Fig. 6b treated according to the selection procedure described in Appendix A. We jointly invert this group velocity curve with different phase velocity branches depicted by the green color symbols. The result corresponding to the first branch (number 1 in Fig. 6c) is displayed in Fig. B.1a where the ERROR value is 0.02802. Similar inversion is repeated for the other phase velocity branches in Fig. 6c (i.e., numbers 2, 3 and 4) and the corresponding results are illustrated in Figs. B.1b, B.1c, and B.1d, respectively. The minimum ERROR value is sought as obtained in Fig. B.1b (i.e., 0.00812), which corresponds to number 2. This Love phase velocity

dispersion curve along with the relevant Love group velocities are marked as valid and are moved to the data repository. The same inversion methodology is applied to the Rayleigh surface waves as shown in Fig. B.2. The group velocity curve (black color symbols) attained from the MFT diagram in Fig. 6e is handled with respect to the selection procedure described in Appendix A. Different phase velocity branches (green color symbols) are obtained from Fig. 6f (i.e., numbers 1, 2, 3 and 4) and are jointly inverted with the group velocity dispersion curve. We seek the minimum ERROR value, which is obtained in Fig. B.2b (i.e., 0.00759) corresponding to the phase velocity branch of number 2. The automatic selection procedure marks this Rayleigh phase velocity dispersion curve as valid and moves it to the data repository along with the relevant Rayleigh group velocities.

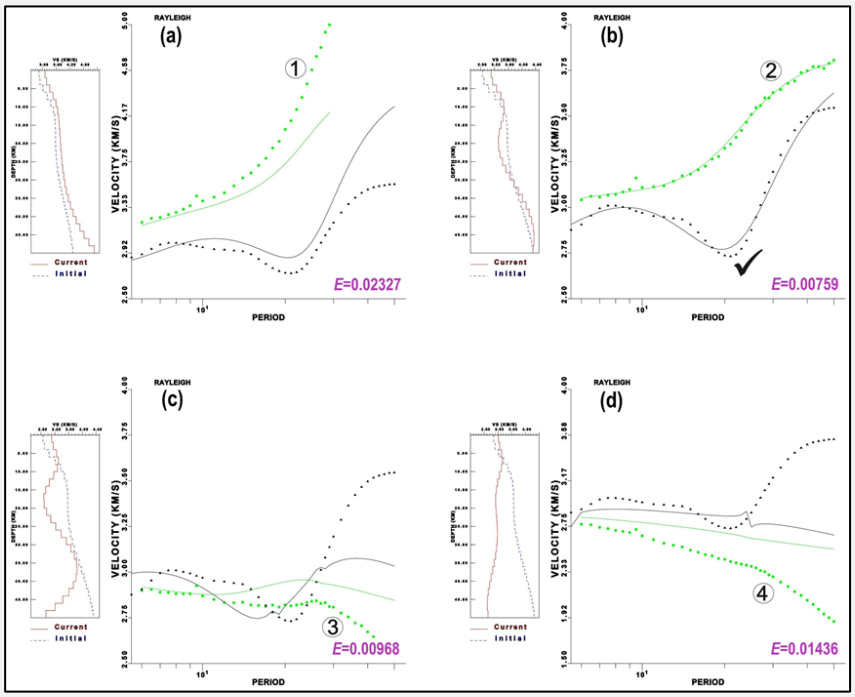

Figure B.2. The two-station selection procedure based on the joint inversion of phase and group velocities is shown for the Rayleigh surface waves. The panel arrangement is the same as in Fig. B.1. Different phase velocity branches defined by 1, 2, 3 and 4 refer to Fig. 6f.

Although rarely needed, we impose a threshold on the minimum ERROR value, i.e., not all minimum ERROR values are accepted. The joint inversions with the minimum ERROR value greater than 0.06 are rated unusable meaning that the group and phase velocities are not compatible with each other, which most likely results from errors in the computation of group and phase velocities. As mentioned in Appendix A, we require that the minimum dispersion curve length is 8-s. Otherwise these joint inversions such as shown in Figs. B.1 and B.2 sometimes get interrupted because of divergence due to the insufficient data (i.e., underdetermined inversion system). In Fig. B.3, we show another example of the two-station phase and group velocity procedure. In this example, the automatic procedure failed to select the dispersion data mainly because of the MFT diagrams in Figs. B.3b and B.3e both not containing the valid group velocity dispersion curves and then the whole selection procedure was abandoned.

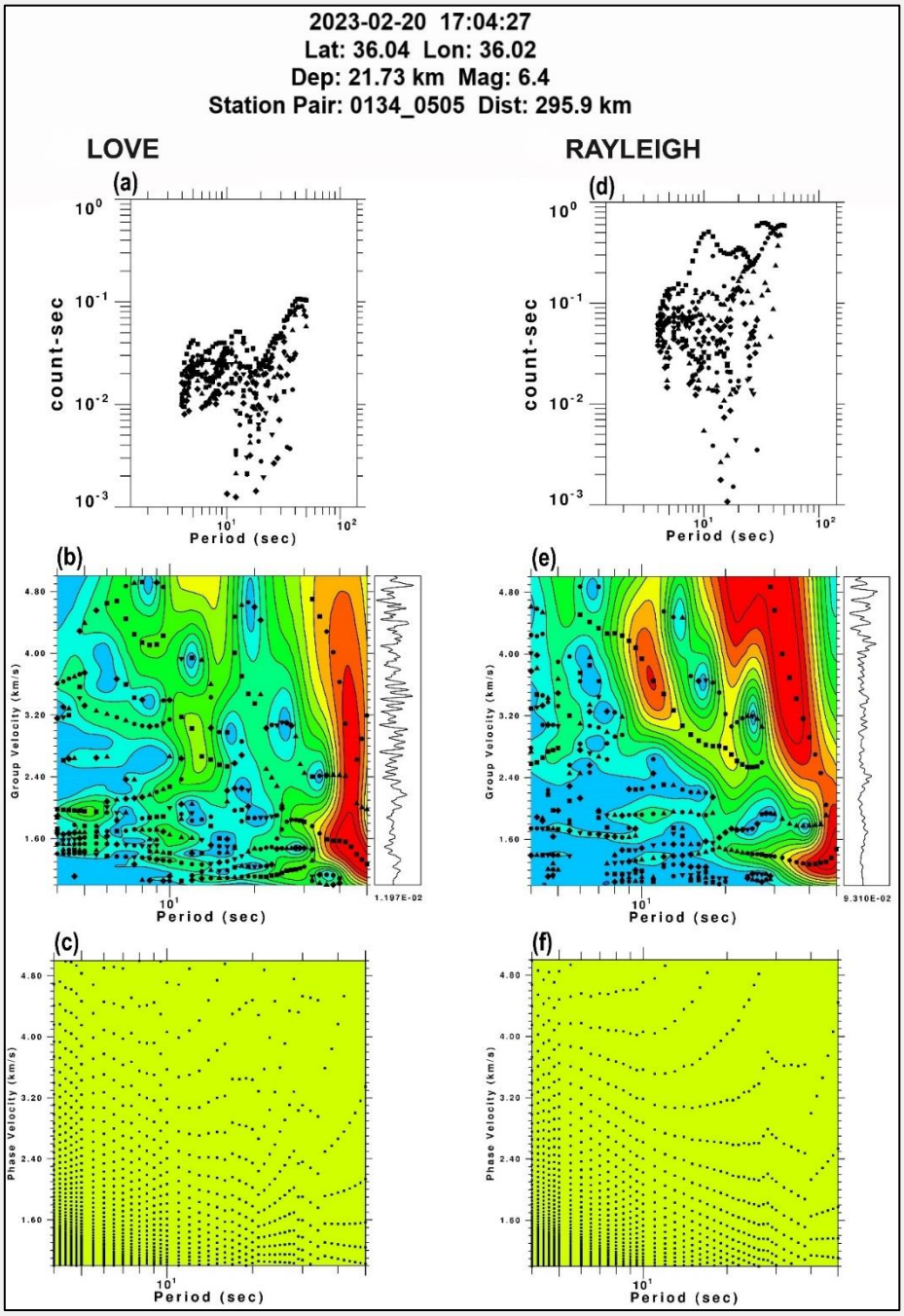

Figure B.3. Failed examples of the two-station analysis applied to the observed Love (left – a, b and c) and Rayleigh (right – d, e and f) surface waves are shown for a station pair between accelerogram stations 0134 and 0505.

Appendix C: More examples regarding the second selection procedure applied to the Rayleigh and Love phase velocities

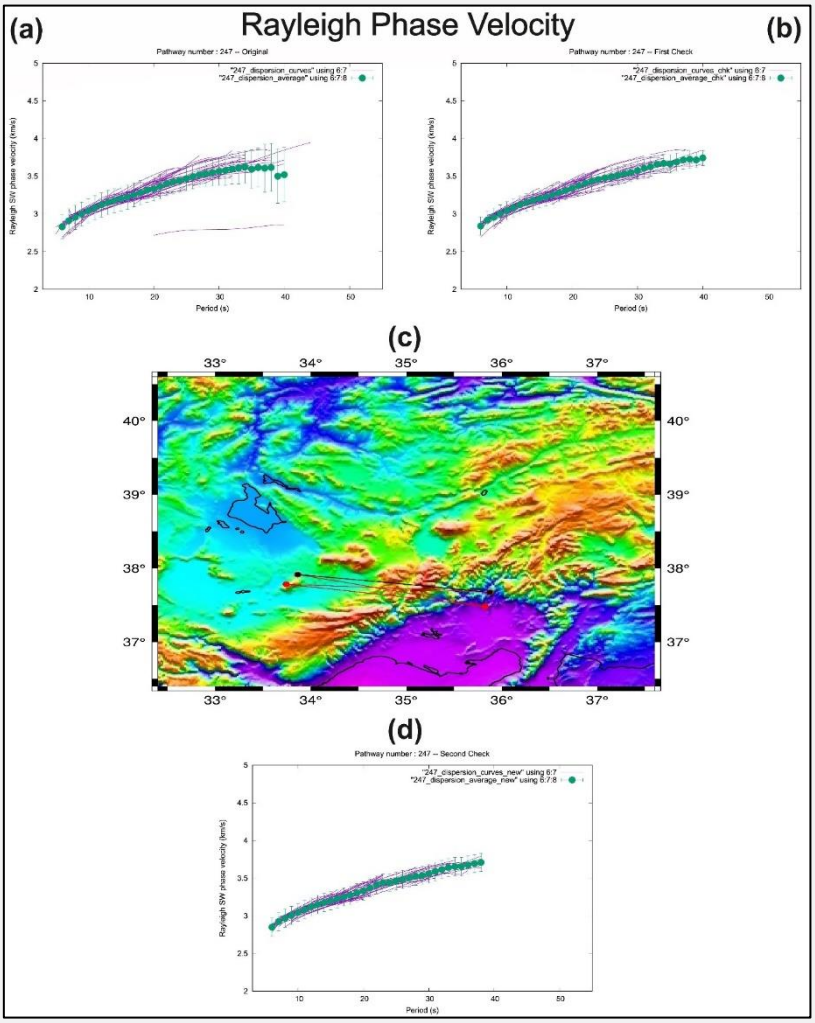

Figure C.1. The second selection procedure applied to multiple Rayleigh phase velocity curves are shown. The propagation pathways (c), original dispersion curves (a), the dispersion curves after the first check (b), and the dispersion curves after the second check (d).

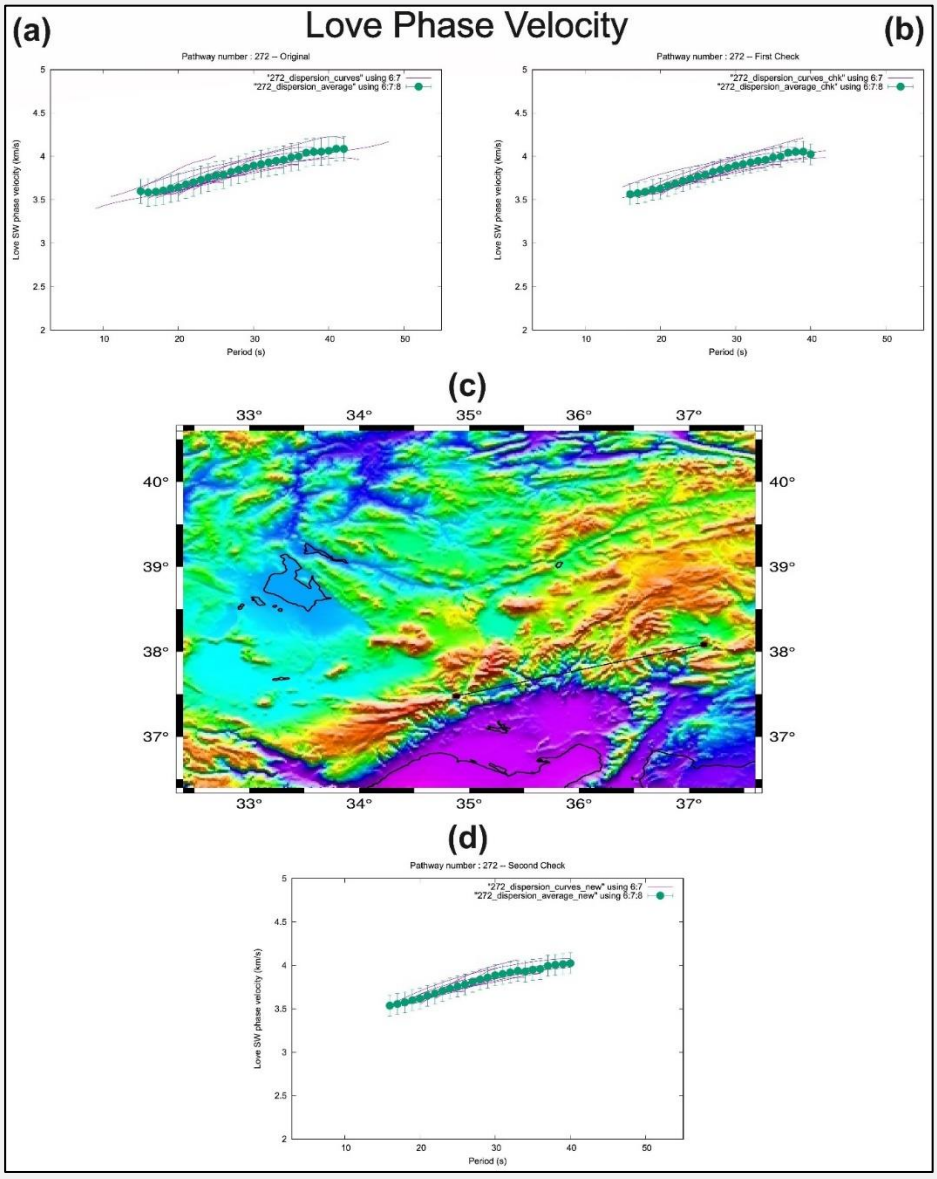

Figure C.2. The second selection procedure applied to multiple Love phase velocity curves.

Appendix D: More examples regarding the two-dimensional (2-D) Rayleigh and Love group velocity maps

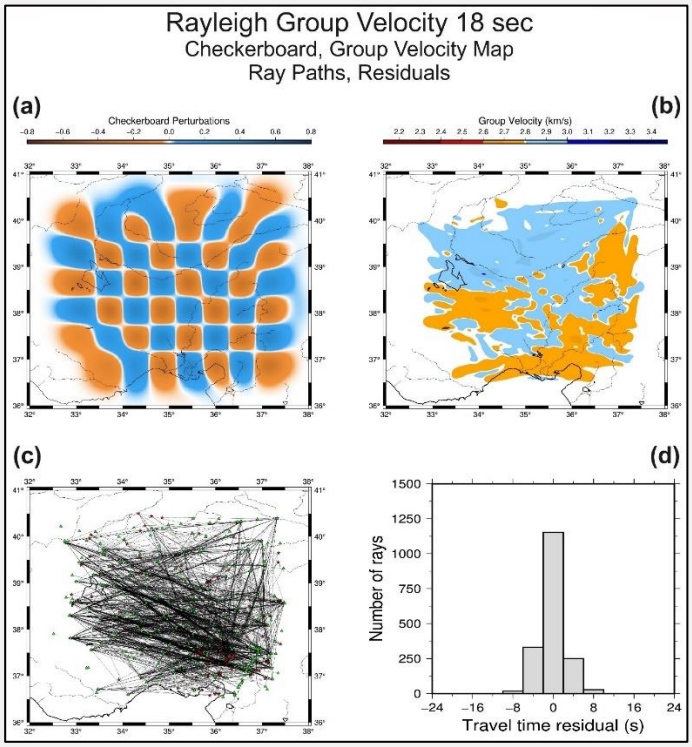

Figure D.1. Group velocity tomography result for 18-s Rayleigh surface waves. The panel arrangement is the same as in Fig. 15.

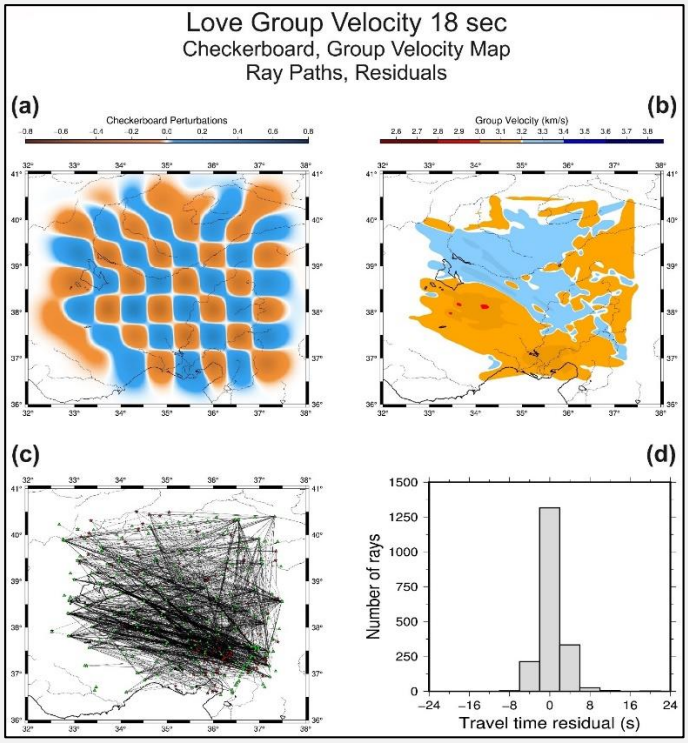

Figure D.2. Group velocity tomography result for 18-s Love surface waves is shown. The panel arrangement is the same as in Fig. 15.

Appendix E: Another example regarding the Rayleigh and Love dispersion inversions for the one-dimensional (1-D) velocity-depth profiles

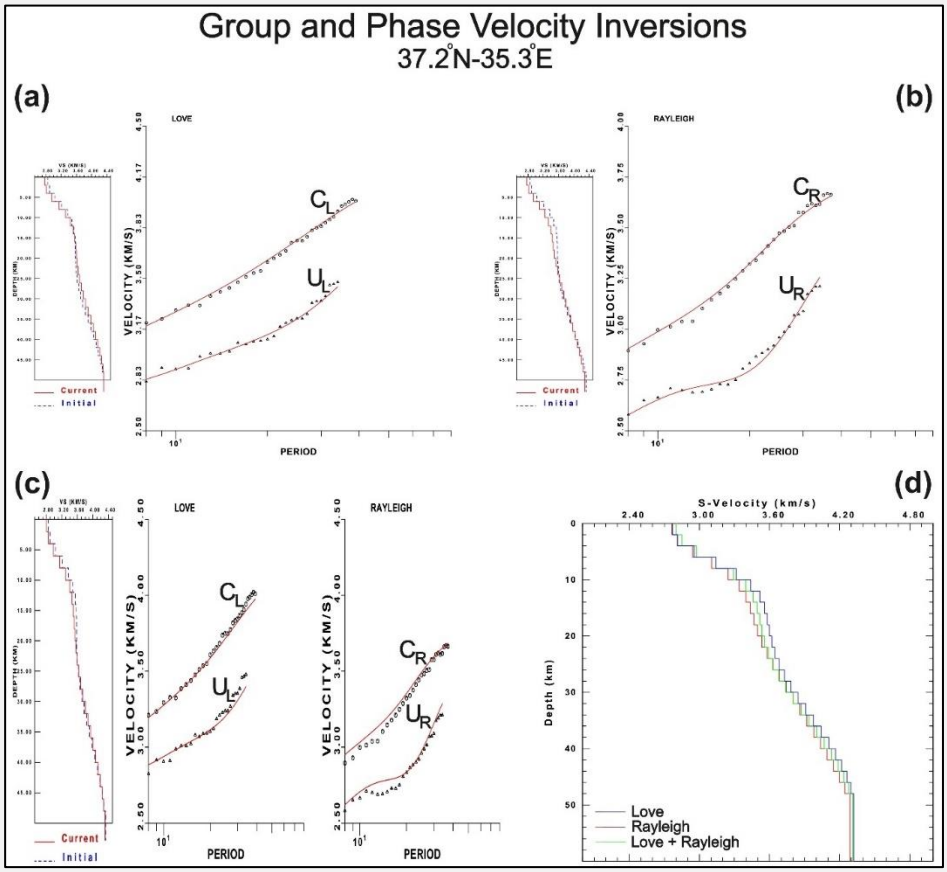

Figure E.1. Inverted shear-wave velocity-depth profiles. Relevant geographic location (37.2° N, 35.3° E) is given in the upper row. The panel arrangement is the same as in Fig. 17.